Simulating heavy neutral leptons with general couplings at collider and fixed target experiments

Jonathan L. Feng,[1,*] Alec Hewitt,[1,†] Felix Kling,[2,‡] and Daniel La Rocco[1,§]

[1]*Department of Physics and Astronomy, University of California, Irvine, California 92697, USA*
[2]*Deutsches Elektronen-Synchrotron DESY, Notkestr. 85, 22607 Hamburg, Germany*

(Received 11 June 2024; accepted 5 July 2024; published 26 August 2024)

Heavy neutral leptons (HNLs) are motivated by attempts to explain neutrino masses and dark matter. If their masses are in the MeV to several GeV range, HNLs are light enough to be copiously produced at collider and accelerator facilities, but also heavy enough to decay to visible particles on length scales that can be observed in particle detectors. Previous studies evaluating the sensitivities of experiments have often focused on simple but not particularly well-motivated models in which the HNL mixes with only one active neutrino flavor. In this work, we accurately simulate models for HNL masses between 100 MeV and 10 GeV and arbitrary couplings to e, μ, and τ leptons. We include over 150 HNL production channels and over 100 HNL decay modes, including all of the processes that can be dominant in some region of the general parameter space. The result is `HNLCalc`, a user-friendly, fast, and flexible library to compute the properties of HNL models. As examples, we implement `HNLCalc` to extend the `FORESEE` package to evaluate the prospects for HNL discovery at forward LHC experiments. We present sensitivity reaches for FASER and FASER2 in five benchmark scenarios with coupling ratios $|U_e|^2:|U_\mu|^2:|U_\tau|^2 = 1:0:0$, $0:1:0$, $0:0:1$, $0:1:1$, and $1:1:1$, where the latter two have not been studied previously. Comparing these to current constraints, we identify regions of parameter space with significant discovery prospects.

DOI: 10.1103/PhysRevD.110.035029

I. INTRODUCTION

The Standard Model (SM) is a remarkably successful theory of particle physics and includes all of the observed particles in nature. However, it does not explain all of the observed phenomena in nature, and hence it is incomplete. In particular, the SM does not accommodate the observed neutrino masses and mixings, and none of the particles it includes can be a significant fraction of dark matter.

Among the simplest ways to extend the SM is to introduce additional fermions that are uncharged under all SM gauge symmetries. Such fermions, known as sterile or right-handed neutrinos, immediately open avenues for addressing the aforementioned problems of the SM. For neutrino masses, the introduction of sterile neutrinos leads to the appearance of neutrino masses and mixings, as required by experimental observations. For dark matter, the coupling of sterile neutrinos to the SM through Yukawa couplings is the unique way that a dark fermion, that is, a fermion with no SM interactions, can interact with the SM through a renormalizable coupling, making it an especially important example of beyond-the-SM (BSM) physics.

Once sterile neutrinos are introduced, they generically mix with the SM neutrinos, and the resulting mass eigenstates are often referred to as heavy neutral leptons (HNLs). HNLs are mostly sterile, but their small SM neutrino components imply that they do interact with SM gauge bosons, which may lead to observable signals. Which signals are possible depends heavily on the HNL mass. Mass scales that have been discussed at length in the literature include ∼eV masses, motivated by experimental anomalies; ∼keV masses, motivated by cosmology and possible evidence for warm dark matter; and masses at the TeV scale and above, motivated by models of leptogenesis and the seesaw mechanism. For reviews, see, for example, Refs. [1–4].

In this work, we consider HNLs with masses in the MeV to GeV range. Such HNLs have attracted interest since at least the early 1970s [5,6]; for a review that includes references to the early literature, see Ref. [7]. In recent years, however, there has been a resurgence of interest in HNLs with masses in the MeV to GeV range. HNLs with such masses may be used to generate neutrino masses and mixings consistent with experimental measurements and

*Contact author: jlf@uci.edu
†Contact author: ahewitt1@uci.edu
‡Contact author: felix.kling@desy.de
§Contact author: laroccod@uci.edu

simultaneously address many of the cosmological problems of the SM; see, for example, Ref. [8]. More generally, from a purely phenomenological perspective, such HNLs are amenable to a wide variety of experimental probes, since they are light enough to be copiously produced at many collider and accelerator facilities, but also heavy enough to decay to visible particles on length scales that can be observed in particle detectors [9–17]. For these reasons, HNLs have become a leading example of long-lived particles (LLPs), and they have helped motivate the growing worldwide research program in search of LLPs.

To evaluate the prospects for HNL discovery, it is essential to have a user-friendly, fast, and flexible tool that can model HNL production and decay and also be used to estimate event rates in current and proposed experiments. The number of production channels and decay modes that may be important for HNLs dwarfs the corresponding number for dark photons and other well-known LLPs. Thankfully, a great deal of work has been done to identify and quantify the leading production and decay processes [10–12,15,16,18–21]. Building on this work, in this study we present the PYTHON library `HNLCalc`, which computes the properties of general HNL models.[1] It includes all of the potentially dominant processes and accurately describes the production and decay of HNLs with $\mathcal{O}(\mathrm{GeV})$ masses and arbitrary couplings to the e, μ, and τ leptons.

HNLs may be produced in both fixed-target and particle collider experiments. Fixed-target experiments may produce many HNLs in the MeV to GeV range, and it is certainly of interest to predict the sensitivity of current and proposed experiments for general HNL searches. At the same time, particle colliders like the LHC are also of interest, particularly in the forward direction, where event rates for such HNLs are greatly enhanced. Our results may be used to model general HNL models and determine discovery prospects at both accelerator and collider experiments.

As examples, in this study we consider the Forward Search Experiment (FASER) [22,23], a current experiment that is purpose built to search for LLPs in the far-forward region at the LHC, and FASER2, a future experiment to be housed in the proposed Forward Physics Facility (FPF) [24,25] at the High-Luminosity LHC (HL-LHC), which will have an even greater discovery potential for LLPs. For forward physics experiments at colliders, the FORward Experiment SEnsitivity Estimator (`FORESEE`) [26] simulation package has become a very useful tool. For a fixed proton-proton c.m. energy, `FORESEE` takes as input the forward hadron production rates given by Monte Carlo (MC) generators, determines the resulting energy and angular distribution for various LLPs, and then calculates the signal rate in particle detectors. `FORESEE` modules have been written to simulate a variety of LLPs, including dark photons, other gauge bosons, and also scalars, but, before this work, not HNLs. In this work, we extend `FORESEE` to simulate HNLs, using the HNL properties provided by the `HNLCalc` package. We focus on models with Majorana-like HNLs in which total lepton number L is violated.

To illustrate the flexibility of both `HNLCalc` and the `FORESEE` HNL module, we analyze the sensitivity reach for five benchmark models, where the ratios of HNL couplings are

$$\begin{array}{lccccc} & |U_e|^2 & : & |U_\mu|^2 & : & |U_\tau|^2 \\ \text{Benchmark 1}: & 1 & : & 0 & : & 0, \\ \text{Benchmark 2}: & 0 & : & 1 & : & 0, \\ \text{Benchmark 3}: & 0 & : & 0 & : & 1, \\ \text{Benchmark 4}: & 0 & : & 1 & : & 1, \\ \text{Benchmark 5}: & 1 & : & 1 & : & 1. \end{array} \tag{1}$$

We refer to these benchmarks using the convenient shorthand 100, 010, 100, 011, and 111. The 100, 010, and 001 models are simple cases, each with only one nonzero coupling, and they are among the benchmarks typically considered, for example, by the Physics Beyond Colliders study group [27]. The reach for FASER in these scenarios was analyzed previously in Refs. [28–30], and we reproduce these earlier results. The 011 and 111 models are less minimal, but have been proposed as more representative of models that explain the observed neutrino masses and mixings [31]. The reach for FASER and FASER2 in the 011 and 111 models has not been determined previously, but is analyzed here rather easily, given the flexibility of the work described here. We note that sensitivities for models with more than one nonzero coupling cannot be estimated simply by adding together event rates from the 100, 010, and 001 models, since all couplings enter the decay width, and so turning on a second or third coupling impacts both the event rates and the kinematic distributions of events mediated by the first coupling in highly nontrivial ways. This interplay can only be included through the detailed simulation work described here.

This paper is organized as follows. In Sec. II we discuss the HNL model and establish the notation we use. In Secs. III and IV we discuss the many HNL production and decay processes, respectively, and describe the detector and collider configurations we consider in Sec. V. In Sec. VI we use all of these results to determine the sensitivity and discovery prospects for FASER and FASER2 in the five benchmark models discussed above. We collect our conclusions in Sec. VII. Detailed expressions for the production and decay branching fractions are contained in Appendices A and B, respectively. In the course of this work, typos and errors in the existing literature were identified, and these are noted in the Appendices.

[1] `HNLCalc` is publicly available on GitHub at https://github.com/laroccod/HNLCalc.

II. MODEL

In this paper, we consider the SM, with its three left-handed active neutrinos, extended to include n right-handed sterile neutrinos. With these extra states, the SM Lagrangian can be supplemented by additional gauge-invariant terms, such as

$$\mathcal{L} \supset -\sum_{\alpha i} y_{\alpha i} \bar{L}_\alpha \tilde{\phi} N'_i - \sum_{ij} m_{ij} \overline{N'^c_i} N'_j - \sum_{\alpha\beta} \frac{1}{M} \lambda_{\alpha\beta} \bar{L}_\alpha \tilde{\phi} \tilde{\phi}^T L^c_\beta + \text{H.c.}, \tag{2}$$

where the fields are the SM left-handed lepton doublets $L_\alpha = (\nu_\alpha, l_\alpha)^T$; the right-handed sterile neutrinos N'_i, where the prime distinguishes the gauge eigenstates from the unprimed mass eigenstates to be defined below; the SM Higgs doublet ϕ; and their charge conjugates $L^c = C\bar{L}^T$, $N'^c = C\overline{N'}^T$, and $\tilde{\phi} = i\sigma_2\phi^*$. The fermion fields ν_α, l_α, and N'_i are each four-component Weyl spinors [e.g., $N'_i = (0, N'_{iR})^T$]; the index sums are over $\alpha, \beta = e, \mu, \tau$ and $i, j = 1, \ldots, n$; $y_{\alpha i}$ and $\lambda_{\alpha\beta}$ are dimensionless (Yukawa) couplings; and m_{ij} and M are mass parameters.

The terms in the first sum in Eq. (2) are the neutrino Yukawa couplings, the only gauge-invariant and renormalizable terms that can couple SM fields to gauge singlet fermions. The terms in the second sum are right-handed Majorana neutrino mass terms, which break total lepton number L. Last, the terms in the third sum also break L, but do not involve the N'_i fields. These terms are nonrenormalizable, but can be generated once heavy singlet neutrinos are integrated out as, for example, in the seesaw mechanism. Similar L-violating terms may also be present even at the renormalizable level if one introduces additional fields, such as a scalar field that is a triplet of SU(2).

After electroweak symmetry breaking, when the neutral component of the Higgs field obtains a vacuum expectation value, the terms of Eq. (2) all contribute to neutrino masses. In the basis (L_α, N'^c_i), the most general $(3+n, 3+n)$ mass matrix is

$$M^\nu = \begin{pmatrix} M_L & M_D \\ M_D^T & M_R \end{pmatrix}, \tag{3}$$

where M_D, M_R, and M_L are the Dirac, right-handed Majorana, and left-handed Majorana masses generated by terms in the first, second, and third sums of Eq. (2), respectively. When the mass matrix M^ν is diagonalized, the resulting mass eigenstates are $3+n$ Majorana neutrinos. These include the three mostly active neutrinos that have been observed experimentally, ν_1, ν_2, and ν_3, and the n mostly singlet HNLs, which we denote as N_i, where $i = 1, \ldots, n$.

In this study, for simplicity, we consider models in which the phenomenology is dominated by a single HNL, which we denote as N, while others either contribute subdominantly or are outside the mass range of interest. Note, however, that we do not assume that the N's mixing is dominated by mixing with only one active neutrino. We consider the N field to have a mass in the MeV to GeV range, and so a wealth of existing observables such as the width of the Z boson constrain their mixings with the active neutrinos to be small. Barring rather special scenarios, such as where the HNLs are almost mass-degenerate and can oscillate into each other on relevant length scales [32,33], the signal rates for HNLs in models with two or more HNLs with significant mixings can therefore be determined simply by adding together the signal rates for each HNL considered separately.

With these simplifications, then, the neutrino flavor eigenstates can be expressed in terms of the mass eigenstates as

$$\nu_\alpha = \sum_{i=1}^{3} V_{\alpha i} \nu_i + U_\alpha N^c, \tag{4}$$

where $V_{\alpha i}$ and U_α parametrize the active and sterile neutrino content, respectively. Therefore, the SM couplings of the electroweak gauge bosons to neutrino flavor eigenstates induce couplings to N proportional to U_α. The charged-current (CC) and neutral-current (NC) interaction terms are

$$\mathcal{L}^{\text{CC}} = -\frac{g}{\sqrt{2}} \sum_\alpha U^*_\alpha W^+_\mu \overline{N^c} \gamma^\mu l_\alpha + \text{H.c.},$$
$$\mathcal{L}^{\text{NC}} = -\frac{g}{2\cos\theta_W} \sum_\alpha U^*_\alpha Z_\mu \overline{N^c} \gamma^\mu \nu_\alpha + \text{H.c.} \tag{5}$$

The production and decay rates for the HNL are completely determined by the mass m_N and couplings U_α. As noted in Sec. I, in this study we consider benchmark models with fixed coupling ratios $|U_e|^2 : |U_\mu|^2 : |U_\tau|^2$ defined in Eq. (1). The only remaining freedom, then, is the overall size of these couplings, which we parametrize by ϵ, the sum of the U_α couplings in quadrature:

$$\epsilon^2 = |U_e|^2 + |U_\mu|^2 + |U_\tau|^2. \tag{6}$$

With these definitions, given a particular benchmark model, the HNL phenomenology is completely determined by the two parameters

$$m_N, \quad \epsilon. \tag{7}$$

We present all of our results below, including the sensitivity reaches of various experiments, as functions of one of these two parameters or in the (m_N, ϵ) plane.

TABLE I. HNL production processes included in `HNLCalc`. The processes are ordered by increasing parent particle mass; P, V, and H denote pseudoscalar mesons, vector mesons, and hadrons, respectively; $l = e, \mu, \tau$; and N is the HNL. Charge-conjugate processes are also implemented but are not explicitly listed here. Representative Feynman diagrams for these processes are shown in Fig. 1.

HNL production processes							
$P \to lN$	Fig. 1(a)	$\pi^+ \to l^+N$	$K^+ \to l^+N$	$D^+ \to l^+N$	$D_s^+ \to l^+N$	$B^+ \to l^+N$	$B_c^+ \to l^+N$
$P \to P'lN$	Fig. 1(b)	$K^+ \to \pi^0 l^+N$	$K_S \to \pi^+ l^-N$	$K_L \to \pi^+ l^-N$	$D^0 \to K^- l^+N$	$\bar{D}^0 \to \pi^+ l^-N$	$D^+ \to \pi^0 l^+N$
		$D^+ \to \eta l^+N$	$D^+ \to \eta' l^+N$	$D^+ \to \bar{K}^0 l^+N$	$D_s^+ \to \overline{K^0} l^+N$	$D_s^+ \to \eta l^+N$	$D_s^+ \to \eta' l^+N$
		$B^+ \to \pi^0 l^+N$	$B^+ \to \eta l^+N$	$B^+ \to \eta' l^+N$	$B^+ \to \bar{D}^0 l^+N$	$B^0 \to \pi^- l^+N$	$B^0 \to D^- l^+N$
		$B_s^0 \to K^- l^+N$	$B_s^0 \to D_s^- l^+N$	$B_c^+ \to D^0 l^+N$	$B_c^+ \to \eta_c l^+N$	$B_c^+ \to B^0 l^+N$	$B_c^+ \to B_s^0 l^+N$
$P \to Vl N$	Fig. 1(b)	$D^0 \to \rho^- l^+N$	$D^0 \to K^{*-} l^+N$	$D^+ \to \rho^0 l^+N$	$D^+ \to \omega l^+N$	$D^+ \to \bar{K}^{*0} l^+N$	$D_s^+ \to K^{*0} l^+N$
		$D_s^+ \to \phi l^+N$	$B^+ \to \rho^0 l^+N$	$B^+ \to \omega l^+N$	$B^+ \to \bar{D}^{*0} l^+N$	$B^0 \to \rho^- l^+N$	$B^0 \to D^{*-} l^+N$
		$B_s^0 \to K^{*-} l^+N$	$B_s^0 \to D_s^{*-} l^+N$	$B_c^+ \to D^{*0} l^+N$	$B_c^+ \to J/\psi l^+N$	$B_c^+ \to B^{*0} l^+N$	$B_c^+ \to B_s^{*0} l^+N$
$\tau \to HN$	Fig. 1(c)	$\tau^+ \to \pi^+ N$	$\tau^+ \to K^+ N$	$\tau^+ \to \rho^+ N$	$\tau^+ \to K^{*+} N$		
$\tau^+ \to l^+\nu N$	Figs. 1(d) and 1(e)	$\tau^+ \to l^+ \bar{\nu}_\tau N$	$\tau^+ \to l^+ \nu_l N$				

III. HNL PRODUCTION

At the LHC, high-energy proton-proton collisions produce hadrons and leptons that can decay to HNLs through the CC and NC interactions of Eq. (5). In the mass range of interest here, HNLs are primarily produced in the decays of mesons and tau leptons. The production of these parent particles at the LHC is modeled using a variety of generators, which are discussed in Sec. V B.

The complete list of all HNL production processes included in this work is given in Table I. They include both two-body and three-body decays, and are divided into six categories: $P \to lN$, $P \to P'lN$, $P \to VlN$, $\tau \to HN$, $\tau^+ \to l^+\bar{\nu}_\tau N$, and $\tau^+ \to l^+\nu_\ell N$, where P, V, and H represent pseudoscalar mesons, vector mesons, and hadrons, respectively. Representative quark-level Feynman diagrams for these processes are given in Fig. 1, and expressions for the corresponding branching fractions are given in Appendix A.

The HNL production processes of Table I include all of the possibly leading contributions. Note that all of the parent hadrons are pseudoscalar mesons. Vector-meson decays do not typically produce HNLs with significant branching fractions because the decays to HNLs compete with decays mediated by the strong interactions and so are highly suppressed. HNL production in baryon decays is also not included, since they are subdominant.

The branching fractions for meson and tau lepton decays into HNLs are presented in Fig. 2 as functions of HNL mass. For illustrative purposes, we show results for the 011 and 111 benchmark models with coupling parameter $\epsilon = 10^{-3}$. For each benchmark model, there are as many as 150 HNL production processes. Rather than show

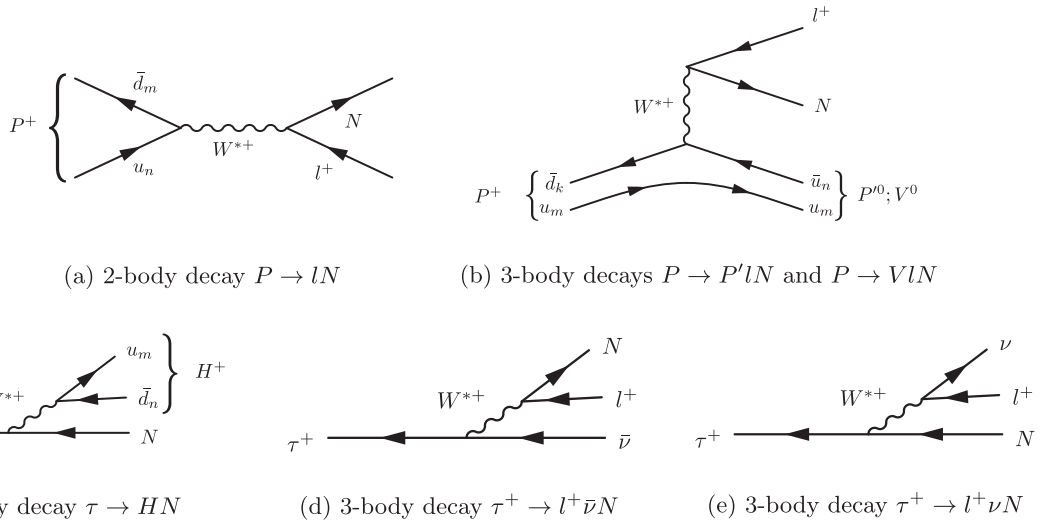

(a) 2-body decay $P \to lN$

(b) 3-body decays $P \to P'lN$ and $P \to VlN$

(c) 2-body decay $\tau \to HN$

(d) 3-body decay $\tau^+ \to l^+\bar{\nu}N$

(e) 3-body decay $\tau^+ \to l^+\nu N$

FIG. 1. Representative Feynman diagrams for the HNL production processes listed in Table I. The subscripts m and n are generation indices.

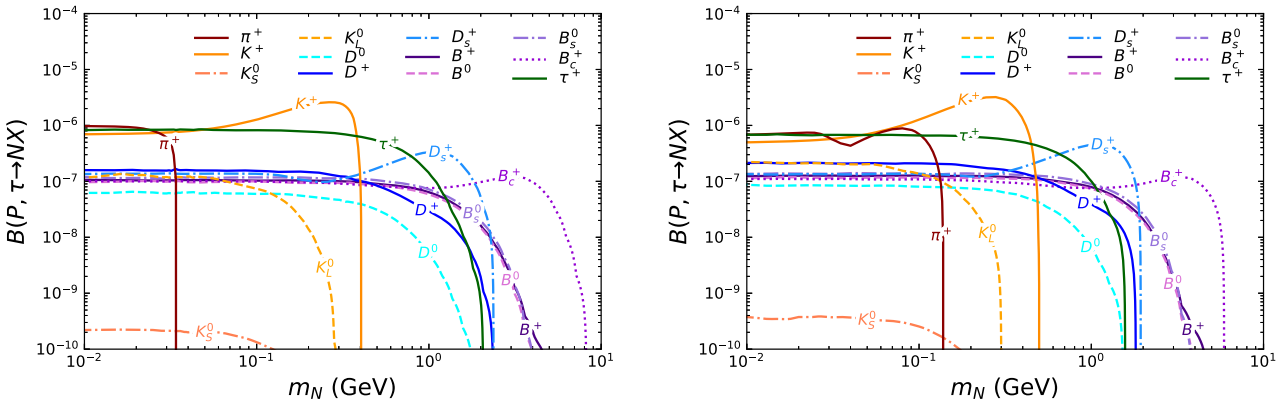

FIG. 2. Branching fractions $B(P, \tau \to NX)$ as functions of the HNL mass m_N for the 011 (left) and 111 (right) benchmarks and $\epsilon = 10^{-3}$. P represents pseudoscalar mesons and NX represents any final state containing the HNL N.

branching fractions for each of these modes, in Fig. 2 we show the total BSM branching fraction for each parent meson, which includes final states with all possible hadrons and lepton flavors.

Because the total branching fractions include many modes, distinctive aspects of individual modes are not always apparent. However, we note a few general features:

(1) The branching fractions are typically larger for the longer-lived mesons, where the competing SM decay modes have smaller widths. This implies that the BSM branching fractions are typically larger for the lighter parent mesons.

(2) Of course, the branching fractions vanish when the decay modes become kinematically inaccessible. For example, $B(\pi^+ \to NX)$ vanishes at $m_N = m_{\pi^+} - m_\mu \simeq 34$ MeV for the 011 benchmark and at $m_N = m_{\pi^+} - m_e \simeq 139$ MeV for the 111 benchmark.

(3) At the same time, although for many modes the branching fraction drops as m_N approaches the kinematic threshold, this is not always the case. For parent mesons where the dominant production mode is chirality suppressed, such as for K^+ mesons where the dominant HNL decay mode is $K^+ \to l^+ N$, the branching fraction vanishes for $m_N = 0$ and grows as m_N increases. In these cases, the branching fraction can be large and even maximal very near threshold.

These facts, coupled with the fact that more light mesons than heavy mesons are produced at the LHC, imply that typically the dominant production mechanism for HNLs is decays of the lightest parent mesons for which the decay is kinematically allowed.

In Fig. 2 we fix $\epsilon = 10^{-3}$, a value that is very roughly at the limit of current constraints. We see that branching fractions of 10^{-7} to 10^{-6} are allowed. Given the enormous flux of far-forward mesons at the LHC, this implies that the flux of highly collimated far-forward HNLs can be significant. Of course, to be detected, the HNLs must decay in the detector to a visible final state.

IV. HNL DECAYS

Once produced, HNLs decay to SM final states through the CC and NC interactions of Eq. (5). The complete list of HNL decay modes included in this work is given in Table II. We consider purely leptonic three-body decays, semileptonic two-body decays, and semileptonic three-body decays. Representative Feynman diagrams for each category are shown in Fig. 3. The HNL decay branching fractions are computed using formulas derived in Refs. [14,16], and the expressions for the branching fractions are given in Appendix B.

To properly simulate the response of the detector to an HNL decay, it is important to know and accurately represent its final states. For example, it can make a big difference experimentally whether an HNL decays to states with charged tracks, e.g., $N \to \nu\rho \to \nu\pi^+\pi^-$, or to states with only final-state photons, e.g., $N \to \nu\pi^0 \to \nu\gamma\gamma$. For this reason, it is generally insufficient to specify HNL decays into quarks as it would rely on hadronization tools to obtain hadronic final states. These tools are known not to

TABLE II. HNL decay modes included in `HNLCalc`, where H denotes hadrons. Representative Feynman diagrams for these modes are shown in Fig. 3. Quark level decays, $\nu q\bar{q}$ and $l u\bar{d}$, are used when computing the total hadronic width when $m_N > 1.0$ GeV.

HNL decay modes							
$\nu l^+ l^-$	Fig. 3(a)	$\nu_l e^+ e^-$	$\nu_l \mu^+ \mu^-$	$\nu_l \tau^+ \tau^-$			
$l^\pm \nu_{l'} l'^\mp$	Fig. 3(b)	$l^\pm \nu_e e^\mp$	$l^\pm \nu_\mu \mu^\mp$	$l^\pm \nu_\tau \tau^\mp$			
$\nu_l \bar{\nu} \nu$	Fig. 3(c)	$\nu_l \bar{\nu}_e \nu_e$	$\nu_l \bar{\nu}_\mu \nu_\mu$	$\nu_l \bar{\nu}_\tau \nu_\tau$			
$\nu_l H^0$	Fig. 3(d)	$\nu_l \pi^0$	$\nu_l \eta$	$\nu_l \eta'$	$\nu_l \rho^0$	$\nu_l \omega$	$\nu_l \phi$
$l^\pm H^\mp$	Fig. 3(e)	$l^\pm \pi^\mp$	$l^\pm K^\mp$	$l^\pm D^\mp$	$l^\pm D_s^\mp$	$l^\pm \rho^\mp$	$l^\pm K^{*\mp}$
$\nu_l q\bar{q}$	Fig. 3(d)	$\nu_l u\bar{u}$	$\nu_l d\bar{d}$	$\nu_l s\bar{s}$	$\nu_l c\bar{c}$	$\nu_l b\bar{b}$	
$l^\pm u\bar{d}'$	Fig. 3(e)	$l^- u\bar{d}$	$l^- u\bar{s}$	$l^- u\bar{b}$	$l^+ \bar{u} d$	$l^+ \bar{u} s$	$l^+ \bar{u} b$
		$l^- c\bar{d}$	$l^- c\bar{s}$	$l^- c\bar{b}$	$l^+ \bar{c} d$	$l^+ \bar{c} s$	$l^+ \bar{c} b$

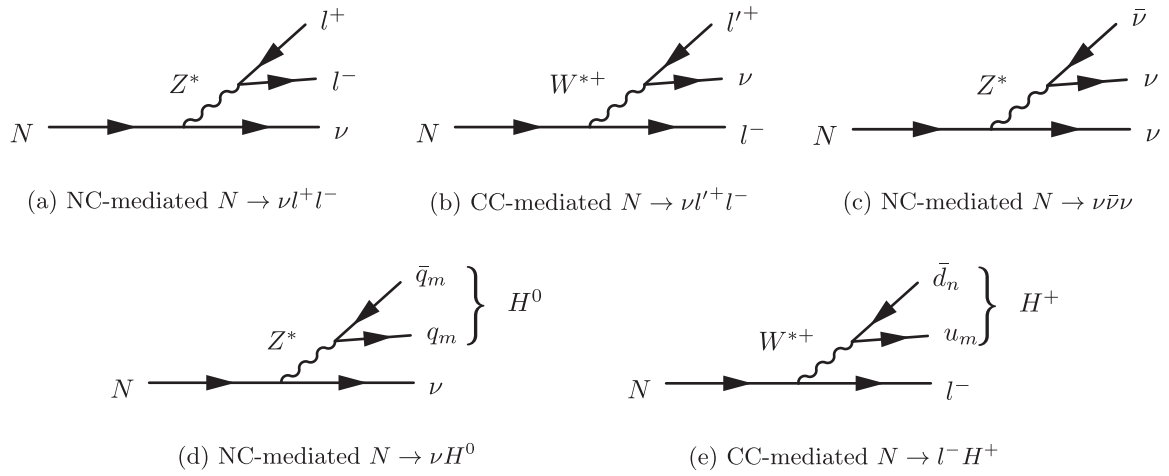

(a) NC-mediated $N \to \nu l^+ l^-$ (b) CC-mediated $N \to \nu l'^+ l^-$ (c) NC-mediated $N \to \nu\bar{\nu}\nu$

(d) NC-mediated $N \to \nu H^0$ (e) CC-mediated $N \to l^- H^+$

FIG. 3. Representative Feynman diagrams for HNL decays. The subscripts m, n are generation indices.

work well when the invariant mass of the hadronic final state is close to or below the QCD confinement scale because, for example, this treatment fails to model hadronic resonances and kinematic thresholds. More generally, in this regime, the factorization theorem loses validity, meaning that one cannot factorize the HNL decay into quarks and use quark hadronization into hadrons anymore. On the other hand, for $m_N \gtrsim 1.0$ GeV, decays into single mesons are insufficient for computing the total HNL decay width, since in this region multimeson decays become important.

To best model hadronic decays at all scales, while also accurately computing the HNL lifetime, we follow the approach taken in Refs. [14,16]. For $m_N < 1.0$ GeV, decays into single mesons, $H = \pi^{\pm,0}, K^{\pm}, \rho^{\pm,0}, \omega, K^{*\pm}, \eta, \eta'$, are calculated using their respective decay constants, f_H, and these are used to obtain the total hadronic decay width. For $m_N \geq 1.0$ GeV, the total hadronic width is instead calculated by summing up HNL decay widths into the quark-level final states $lq\bar{q}'$ and $\nu q\bar{q}$. A QCD loop correction to account for hadronization is applied. This estimated correction is obtained from the known corrections up to $\mathcal{O}(\alpha_s^3)$ in hadronic τ decay; see Appendix B for its explicit form.

Included in our single-meson decays are decays into ρ mesons. It has been shown in Ref. [14] that the dominant source of two-pion final states are decays into ρ mesons followed by $\rho \to \pi\pi$. We therefore take the difference between the quark-level decay width and the single-meson total width as an estimate of the decay width to final states with ≥ 3 hadrons. Additionally, to avoid overestimating the contribution of νss to the hadronic width below the $2m_K$ kinematic threshold, a phase-space suppression factor $\sqrt{1-4m_K^2/m_N^2}$ is applied to this decay. This same approach is also applied to the decays τud and τus, with kinematic thresholds at $m_\tau + 2m_\pi$ and $m_\tau + m_\pi + m_K$, respectively.

In Figs. 4 and 5, we plot the branching fractions for all relevant modes in the 011 and 111 benchmarks. Additionally, the HNL lifetimes are given in Fig. 6.

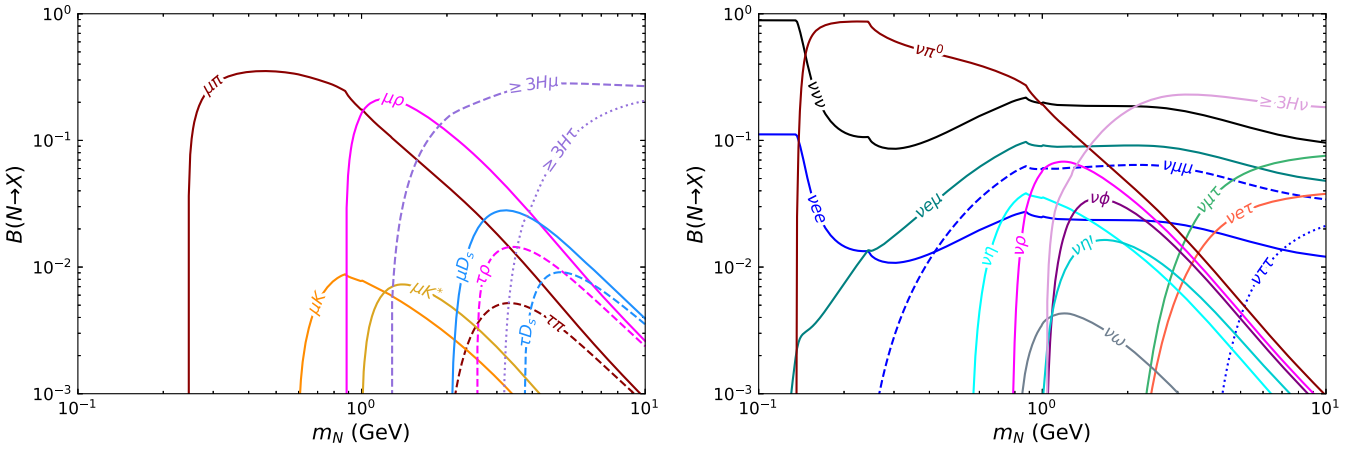

FIG. 4. HNL branching fractions in the 011 benchmark model for the dominant decays via CC (left) and NC (right) interactions as functions of m_N. For $m_N \lesssim 1.0$ GeV the decays are primarily to pions, while for $m_N \gtrsim 1.0$ GeV the decays are dominated by decays to three or more hadrons. Decays to D mesons are subdominant, with $B(N \to lD) < 0.1\%$.

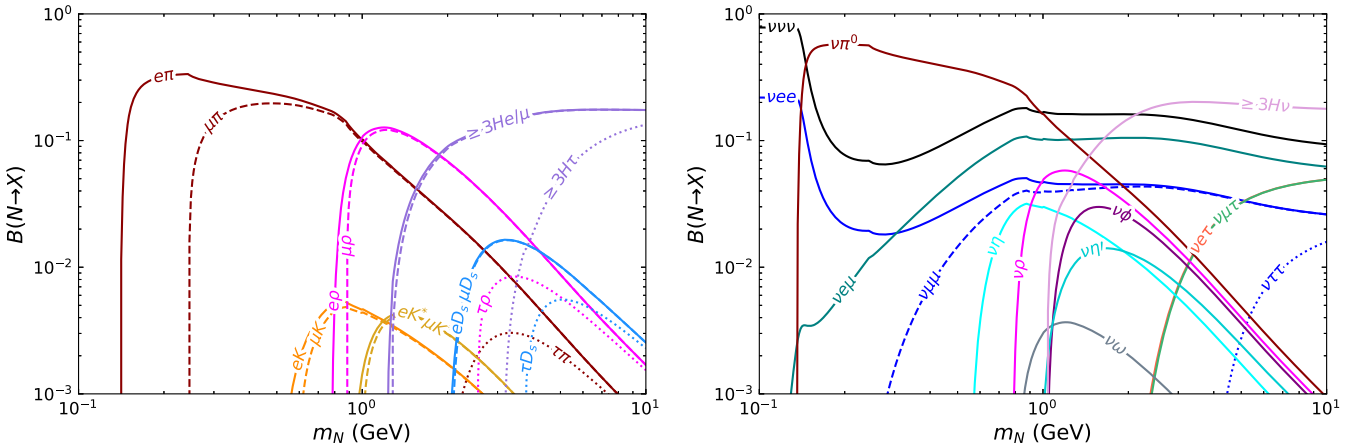

FIG. 5. As in Fig. 4, but for the 111 benchmark model.

For $m_N < m_\pi$, HNL decays are dominated by NC decays into the three-body final states $\nu\bar{\nu}\nu$ and νe^+e^-. The invisible decay mode dominates and the visible branching fraction is only approximately 10% and 20% in the 011 and 111 benchmark models, respectively. However, for $m_N > m_\pi$, the two-body decays $N \to l^\pm\pi^\mp$ and $N \to \nu\pi^0$ become kinematically accessible, resulting in a sharp drop in the lifetime, as seen in Fig. 6. For masses $m_N > m_\pi$, the hadronic decay modes become dominant and the invisible decay branching fraction is below 20% in both scenarios.

It is important to note that in this work we neglect the effects of spin correlations between production and decay. These do not change the HNL lifetimes and event rates, but they can impact the kinematic distributions of the final-state particles. In the case of Majorana HNLs, where lepton-number-conserving and lepton-number-violating processes, for example, $B_c \to \mu^+\mu^+\tau^-\nu$ and $B_c \to \mu^+\mu^+\tau^-\bar{\nu}$, are both possible, interesting effects in kinematic distributions have the potential to differentiate between the two final states, which are otherwise experimentally identical; see, for example, Ref. [34].

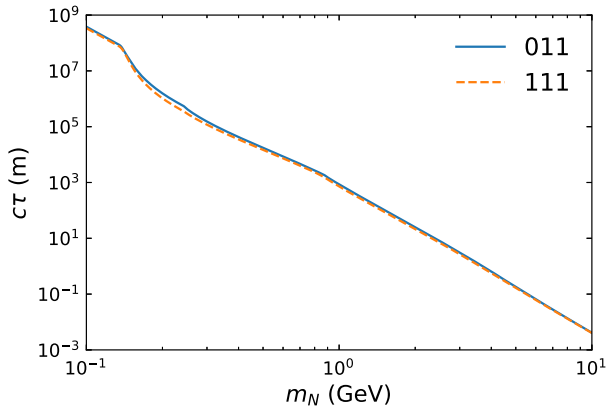

FIG. 6. Lifetimes for the 011 and 111 benchmark models with $\epsilon = 10^{-3}$. A visible kink in the lifetime can be observed at $m_N \approx m_\pi$, where the decay $N \to \nu\pi^0$ becomes kinematically accessible.

V. HNLS AT FASER AND FASER2

In this section, we describe the modeling of meson and τ production at the LHC and the resulting flux of HNLs at FASER [22] and FASER2 [25] during Run 3 and the HL-LHC era. Given the modeling of production and decay of HNLs in Secs. III and IV, respectively, with the use of `HNLCalc`, the `FORESEE` simulation framework can determine the sensitivity for HNL searches with forward detectors at the LHC.

A. Collider and detector setup

FASER is located in a tunnel $L = 480$ m downstream from the ATLAS interaction point (IP). The FASER decay volume is a cylinder with a radius of $R = 10$ cm and a length of $\Delta = 1.5$ m along the beam collision axis. The decay volume extends to angles $\theta \simeq 0.2$ mrad from the beamline and pseudorapidities $\eta \gtrsim 9.2$. We consider the reach of FASER during Run 3 of the LHC with an integrated luminosity of 250 fb^{-1}. We also consider the scenario in which the FASER detector runs throughout the HL-LHC era with an integrated luminosity of 3 ab^{-1}.

In addition, we consider FASER2, one of the experiments proposed for the future FPF [24,25]. FASER2 will be positioned roughly $L = 650$ m away from the ATLAS IP. Its decay volume has length $\Delta = 10$ m and a rectangular cross section with dimensions $3\text{m} \times 1$ m [35]. The FASER2 decay volume extends to angles $\theta \simeq 2.4$ mrad from the beamline and pseudorapidities $\eta \gtrsim 6.7$.

During Run 3, the LHC has operated with a pp c.m. energy of $\sqrt{s} = 13.6$ TeV. For the HL-LHC era, the c.m. energy is expected to be increased to 14 TeV. We find negligible differences in sensitivities from this change in c.m. energy, and for simplicity we assume $\sqrt{s} = 14$ TeV for all results derived here. The detector configurations are summarized in Table III.

TABLE III. Parameters for the three experimental configurations considered: FASER (Run 3), FASER (HL-LHC), and FASER2 (HL-LHC). L is the distance from the IP to the front of the detector, Δ is the length of the detector along the beam axis, Geometry specifies the cross sectional area (cylindrical (cyl.) for FASER, rectangular (rect.) for FASER2), and $\mathcal{L}$ is the integrated luminosity. Both FASER and FASER2 are assumed to be centered on the beam collision axis.

	L	Δ	Geometry	$\mathcal{L}$
FASER (Run 3)	480 m	1.5 m	Cyl. $R = 10$ cm	250 fb^{-1}
FASER (HL-LHC)	480 m	1.5 m	Cyl. $R = 10$ cm	3 ab^{-1}
FASER2 (HL-LHC)	650 m	10 m	Rect. 3 m $\times$ 1 m	3 ab^{-1}

B. HNL production rates at the LHC

HNL production rates at the LHC are obtained in FORESEE through the MC sampling of the decays of parent particles [26]. The spectra for parent pions and kaons are obtained using the dedicated hadronic interaction model EPOS LHC [36]. For charm and bottom hadrons, we use the spectra obtained from POWHEG [37] matched with PYTHIA [38], as presented in Ref. [39]. Tau leptons are produced primarily in charm and bottom hadron decay, so we follow the same prescription there. The primary source of uncertainty on the HNL flux originates from the modeling of hadron production. To estimate this uncertainty, we follow the prescription of Ref. [40] and consider the range of predictions from EPOS LHC, QGSJET 2.04 [41], and Sibyll 2.3d [42] to model the uncertainty for light hadron production, and we take account of scale variations [39] to model the flux uncertainty for heavy hadron production.

The production rates for the 011 and 111 benchmarks at the LHC are shown in Figs. 7 and 8. These figures show the total flux of HNLs produced in the direction of FASER and FASER2, respectively. For FASER, Fig. 7 shows the rate for production with an angle $\theta \leq 0.1$ m/480 m $=$ 0.2 mrad relative to the beam collision axis, and for FASER2, Fig. 8 shows the rate for the production of parent particles that pass through FASER2's 3 m $\times$ 1 m transverse area. As anticipated in Sec. III, the dominant production rate is typically from the lightest meson for which the decay is kinematically accessible. For the 111 scenario, the decay $\pi \to eN$ is possible, and so this is the dominant production process for very light N with masses $m_N \sim 100$ MeV. For the 011 scenario, this decay is not allowed, and pion decays are never dominant for $m_N \gtrsim 100$ MeV. For larger m_N, the results for the 011 and 111 scenarios are similar, with the production rates cutting off as the kaon, tau-lepton, D-meson, and B-meson kinematic thresholds are passed.

C. Signal and background considerations

Depending on their mass, HNLs can decay into a variety of final states, shown in Figs. 4 and 5. The dominant decay channels consist of either two charged particles, such as the decays $N \to \nu l^+ l^-$ and $N \to l^+ \pi^-$, or photons, especially from $N \to \nu\pi^0 \to \nu\gamma\gamma$. The corresponding experimental signatures in the FASER detector would consist of highly energetic charged particles or photons that emerge from the decay volume. The charged particle signal would leave high-momentum tracks in the FASER spectrometer that are consistent with a single vertex inside the decay volume and whose combined momentum points back to the IP. If the final state contains electrons, they would additionally leave a sizable energy deposit in the calorimeter.

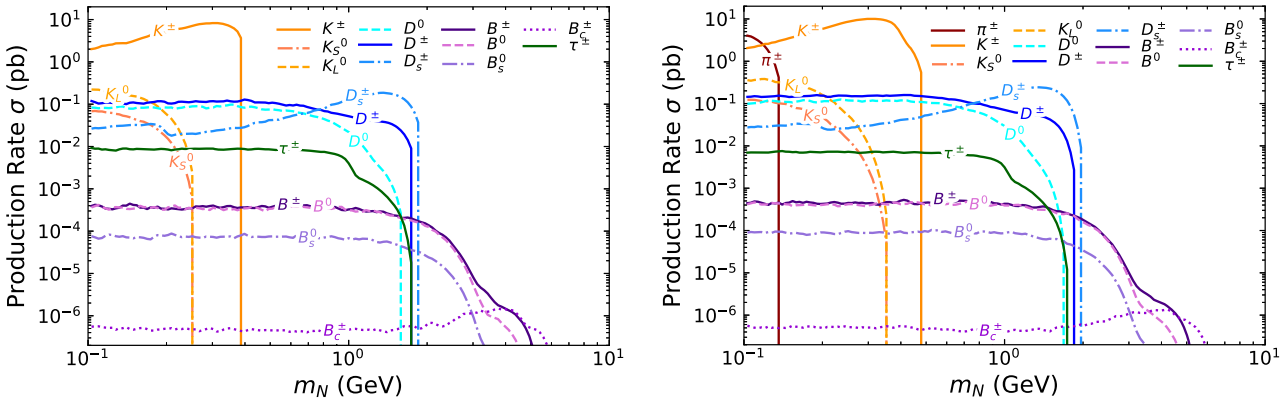

FIG. 7. Production rate of HNLs in the direction of FASER with $\theta < 0.2$ mrad. The rates are grouped by parent particle and are obtained by MC integration in FORESEE for the 011 (left) and 111 (right) benchmarks, with a coupling of $\epsilon = 10^{-3}$.

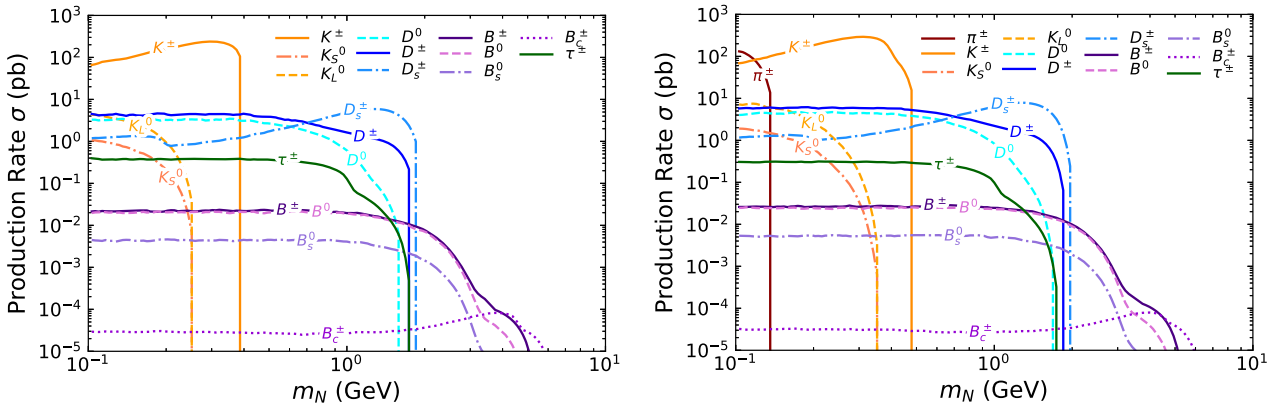

FIG. 8. Production rate of HNLs in the direction of FASER2, that is, that pass through FASER2's transverse area of 3 m × 1 m. The rates are grouped by parent particle and are obtained by MC integration in FORESEE for the 011 (left) and 111 (right) benchmarks, with a coupling of $\epsilon = 10^{-3}$.

The multiphoton signal would leave a characteristic signal in the preshower and deposit a large amount of energy in the calorimeter. In both cases, the signal would not trigger the front veto.

The potential backgrounds for long-lived particle searches at FASER are induced by either high-energy muons or neutrinos coming from the direction of the IP. However, muons are efficiently detected by FASER's front veto, while neutrino interactions are relatively rare and typically have different kinematics. The FASER Collaboration presented their first analysis on dark photons, providing a two-track signal, in which they accounted for a variety of possible background sources associated with veto inefficiencies, neutral hadrons, muons missing the veto, neutrinos, and noncollision background [43]. These backgrounds were determined to be either very small or negligible, and no events with two reconstructed tracks passing the veto requirement have been observed. We therefore assume that backgrounds for multitrack signatures can be considered negligible.

More recently, the FASER Collaboration also presented results for a search for axion-like particles, considering a multiphoton signal [44]. A potentially sizable background from neutrinos interacting at the end of the detector was identified, particularly at energies below 1 TeV. To address this issue, a high-precision preshower upgrade is planned to be installed at the end of 2024, which will allow the experiment to identify multiphoton signatures and differentiate them from neutrino backgrounds [45]. We therefore assume that backgrounds for multiphoton signatures are also negligible.

The design for FASER2 is currently under development [25]. It will have a similar conceptual architecture as the currently operating FASER detector, and background rejection is one of the key considerations for the detector design. Although the design has not yet been finalized, it is envisioned that the same searches will be background free.

VI. REACH

We now present the $N = 3$ signal event contours in the (m_N, ϵ) plane for the various benchmark scenarios. In the absence of background, these may be considered to be discovery contours. The results for the 100, 010, and 011 benchmark models are given in Fig. 9, and the results for the 011 and 111 benchmark models are given in Fig. 10. The signal event rates include all of the production modes listed in Table I and all of the decay modes shown in Table II, except for the invisible decay modes $\nu\bar{\nu}\nu$. Additionally, a momentum cutoff of $p_N > 100$ GeV is applied. The event rates are determined by setting nsample = 25 in the FORESEE MC simulation [26], and the (m_N, ϵ) parameter space is scanned using 100 equally log-spaced masses m_N from 100 MeV to 4 GeV, and 50 equally log-spaced couplings ϵ from 10^{-5} to 1.

Results are presented for the three FASER/FASER2 configurations shown in Table III. The shaded band corresponds to the flux uncertainty, following the prescription in Sec. V B. Sensitivity contours for the 100, 010, and 001 models have been investigated previously [28,30]. Our obtained sensitivities are consistent with these results over most of the mass range. They are slightly improved for $m_N \lesssim m_K$, due to an issue that was found in the kaon decay modes of these previous results. Sensitivity reaches for FASER and FASER2 for the 011 and 111 models have not been determined before.

Various threshold effects can be observed in the sensitivity contours, depending on which production channels dominate HNL production. In the 100 benchmark, the production of HNLs is predominantly governed by pions in the region 100 MeV $\leq m_N \leq m_\pi$, transitions to being dominated by kaons in the range $m_\pi \leq m_N \leq m_K$, shifts to being influenced by D and τ particles within the interval $m_K \leq m_N \leq m_D$, and eventually becomes dominated by B mesons for $m_N \geq m_D$. Additionally, one can infer from the sensitivity contours that the 011 benchmark sensitivity is

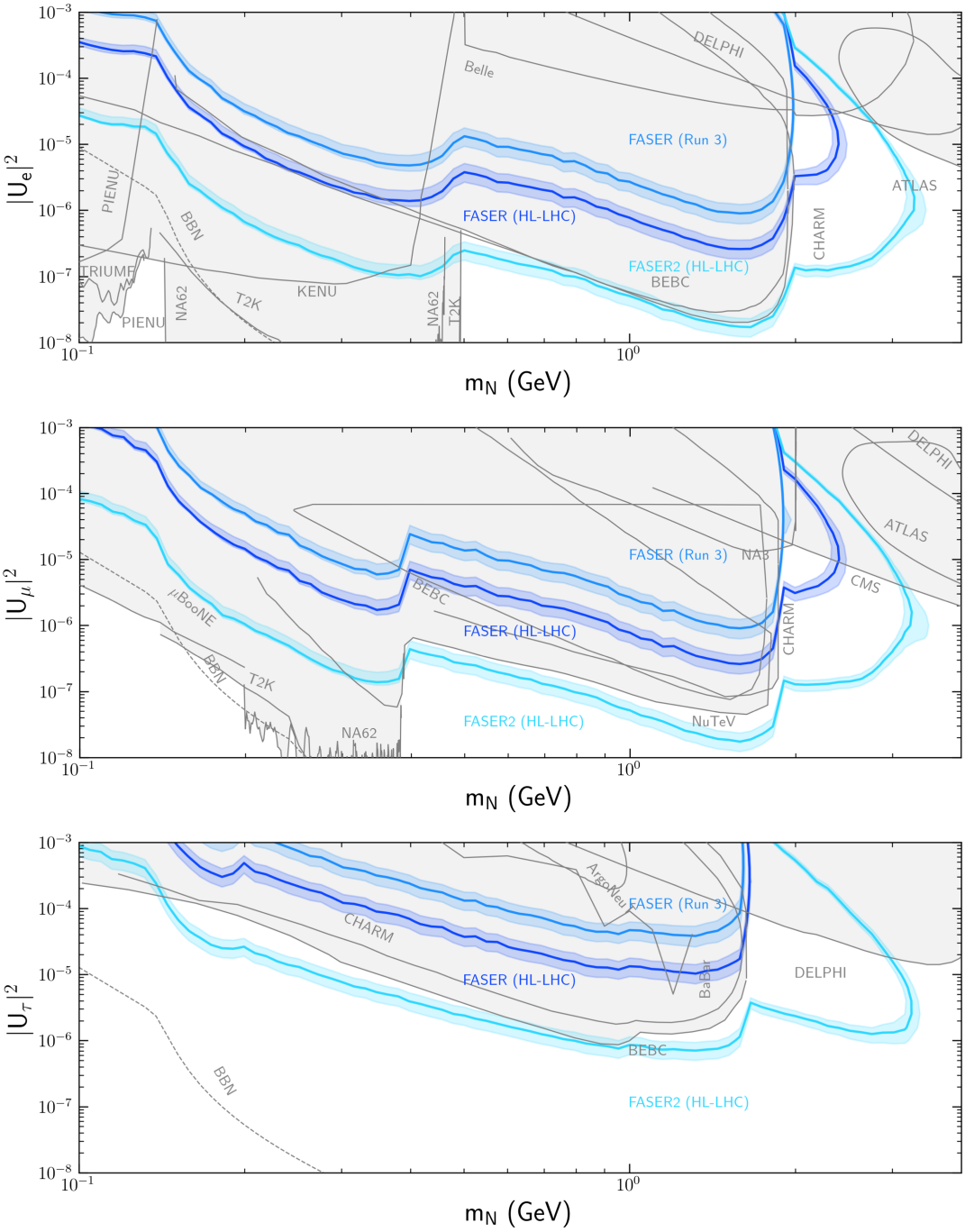

FIG. 9. $N = 3$ signal event contours for the single-coupling 100 (top), 010 (middle), and 001 (bottom) benchmark models. Each blue (bolded) contour corresponds to a detector/collider configuration given in Table III. Current bounds from other particle experiments exclude the gray shaded regions, and BBN constraints exclude the region below the dashed contour. All of the production modes in Table I are included, and all of the decay modes in Table II are included except for the invisible $\nu\bar{\nu}\nu$ modes. For the FASER and FASER2 contours, a momentum cut of $p_N > 100$ GeV is applied.

primarily driven by the U_μ coupling and the 111 benchmark sensitivity is primarily driven by the U_e coupling.

It is, of course, interesting to compare the sensitivity of FASER and FASER2 to current constraints. For the 100, 010, and 001 models, the exclusion bounds have been determined for many past experiments and are available using the PYTHON package HNL-Limits [46]. For the 100 and 001 benchmarks, the BEBC and CHARM bounds in HNL-Limits were refined in Ref. [47] and we adopt those limits. For the 010 benchmark, we use the lower bound provided by the CHARM Collaboration [48]. To establish the upper limit for this benchmark, we use the bounds

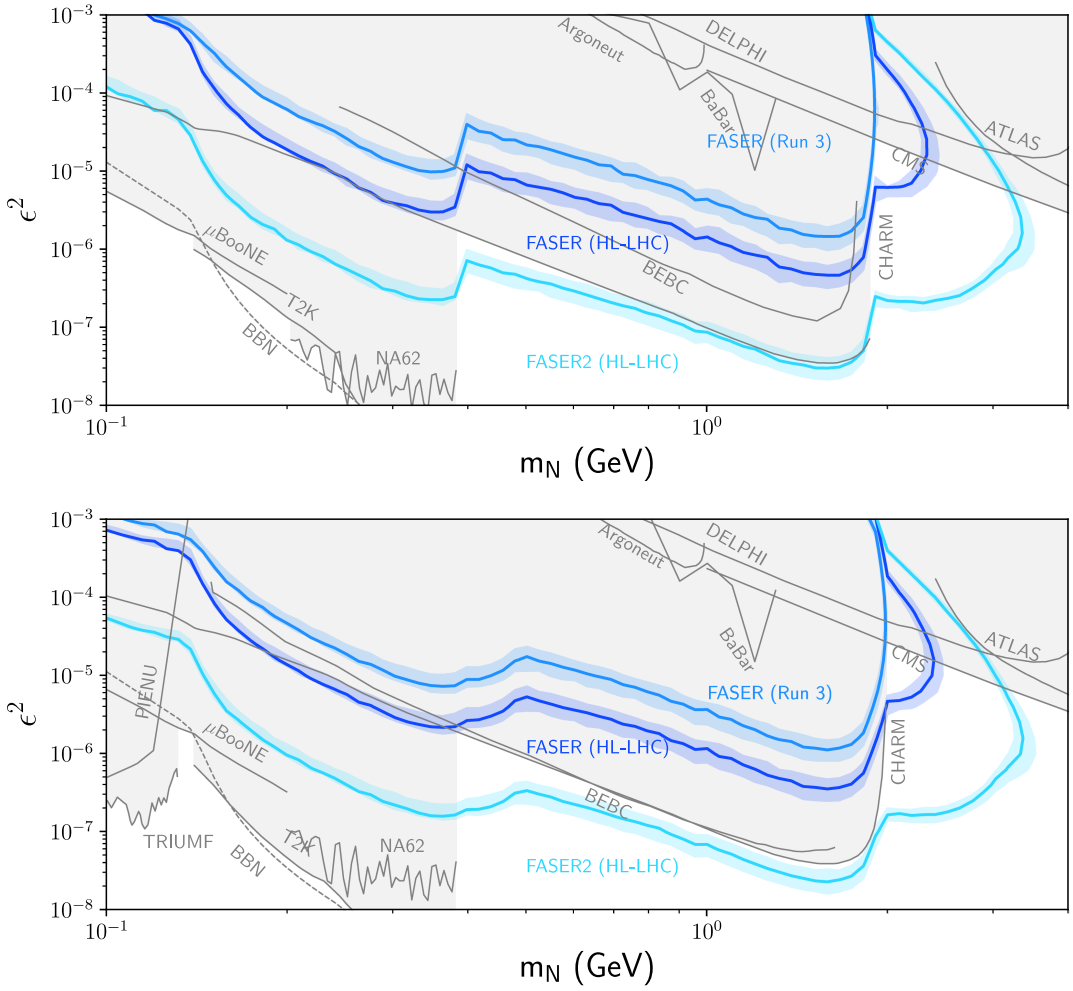

FIG. 10. As in Fig. 9, but for the mixed-coupling 011 (top) and 111 (bottom) benchmark models. In contrast to the single-coupling models, constraints from other experiments are not available in the literature. The current bounds shown in the gray shaded region are roughly estimated based on a method described in the text.

derived for the 100 benchmark model from the CHARM recasting detailed in Ref. [47] as an approximation. We further apply a cutoff at $m_{D_s} - m_\mu$ in the 010 and 011 CHARM bounds to account for the allowed phase space. In addition, for small masses, there are constraints from big bang nucleosynthesis (BBN), which constrains the lifetime of the HNL to be less than 0.1 s [49].

For the 011 and 111 models, the sensitivities of previous experiments are not often found in the literature. To compare FASER and FASER2 to existing constraints, an analysis similar to the one we have done for FASER and FASER2 must be done, requiring a dedicated analysis for each model and experiment. This is beyond the scope of this work. However, we may roughly estimate the sensitivities of previous experiments in the 011 and 111 models by extrapolating their limits in the 100, 010, and 001 models, as we now describe.

In peak search experiments, one looks for evidence of HNL production by searching for peaks in the energy spectrum of coproduced particles. One such example are the bounds placed by the PIENU Collaboration [50], where they performed a search for peaks in the positron energy spectrum in the process $\pi^+ \to Ne^+$. Bounds in these types of experiments place limits on U_α that are independent of the HNL lifetime and decay products and thus will not be effected by the introduction of mixed couplings. The bounds on U_α can therefore be rescaled directly to obtain bounds for ϵ.

In prompt decay or decay-in-flight searches, such as those at ATLAS [51] or CHARM [52], one searches for evidence of HNLs by looking for HNL decay products within the detector. In these experiments, the introduction of mixed couplings can effect the kinematic distributions of final states, as well as the HNL lifetime, causing a change in the overall expected event rate. As a very rough approximation, we can neglect the effect on the kinematics by making the simplifying assumptions that the detector acceptance and efficiency are uniform across all benchmarks. In the long-lifetime limit, then, the expected event rate in these experiments scales as

$$N_\alpha \propto \frac{|U_\alpha|^2}{\tau}, \tag{8}$$

where N_α is the contribution to the total event rate occurring through ν_α mixing. This allows one to relate the expected event rates between the mixed-coupling and single-coupling scenarios by

$$\frac{N_{\alpha,m}}{N_{\alpha,s}} = \frac{|U_{\alpha,m}|^2}{|U_{\alpha,s}|^2}\frac{\tau_s}{\tau_m}, \tag{9}$$

where the subscript m (s) denotes the mixed (single) coupling scenario. Approximate exclusion bounds derived in this way for the 011 and 111 benchmarks are plotted in Fig. 10.

For the sensitivity reaches in the single-coupling scenarios shown in Fig. 9, the results may be summarized as follows. For FASER (Run 3), the reach beyond current bounds is rather modest and is limited to the 100 model. For FASER (HL-LHC), the reach is extended, with discovery prospects in the 100 and 010 scenarios for $m_N \sim 2$ GeV. Finally, for FASER2 (HL-LHC), there are significant regions of parameter space in all three models with sensitivity beyond current bounds. This includes regions of parameter space with $10^{-7} \lesssim \epsilon^2 \lesssim 10^{-5}$ and 2 GeV $\lesssim m_N \lesssim 4$ GeV, where the HNLs are produced in B-meson decays, and also regions of low ϵ at lower m_N. This is especially notable in the 001 scenario, where the new parameter space probed extends all the way down to HNL masses of approximately 150 MeV.

For the sensitivity contours in mixed coupling scenarios shown in Fig. 10, we find that the comparison of the reach of FASER and FASER2 relative to current bounds for the 011 and 111 scenarios approximately mirrors those for the 010 and 100 models, respectively. In particular, for FASER2 (HL-LHC) there is again new parameter space probed with $10^{-7} \lesssim \epsilon^2 \lesssim 10^{-5}$ and 2 GeV $\lesssim m_N \lesssim 4$ GeV, and also improved sensitivity over current bounds at low ϵ and masses 400 MeV $\lesssim m_N \lesssim 2$ GeV. However, we reiterate that in this comparison the FASER and FASER2 bounds derived here are compared to current bounds that have been derived in the very rough way we outlined above. Detailed comparisons require dedicated analyses of the reach of other experiments in these less minimal, mixed-coupling scenarios.

Finally, let us comment on the flux uncertainties, which are shown as shaded bands in Figs. 9 and 10. Despite substantial flux uncertainties, which can be as large as a factor of 2 for charm production, their overall impact on the sensitivity is relatively small. This is due to a strong coupling dependence of the event rate at both small and large couplings. The flux uncertainties mainly affect the reach at the higher mass edge of the sensitivity contour. We note that further measurement, especially the measurement of collider neutrino fluxes, will help to further decrease those flux uncertainties.

VII. CONCLUSIONS

HNLs are well motivated in extensions of the SM designed to address the outstanding puzzles of neutrino masses, dark matter, and baryogenesis. In this work, we comprehensively studied the possibility of probing HNLs with masses in the 100 MeV to 10 GeV range and completely arbitrary mixings with the three active SM neutrinos. We produced a comprehensive package, `HNLCalc`, that computes the properties of the HNL model, including hundreds of production and decay modes. Using `HNLCalc`, we created an HNL module in the `FORESEE` simulation package to evaluate the discovery potential of HNLs in various experimental setups.

In particular, we estimated the sensitivity to HNLs for FASER in Run 3, FASER at the HL-LHC, and FASER2 at the HL-LHC. As an illustration of the flexibility of `HNLCalc`, we considered five benchmark models. For the well-studied 100, 010, and 001 benchmarks, we found that FASER in Run 3 has rather limited discovery prospects. However, FASER at the HL-LHC can probe new parameter space with $m_N \sim 2$ GeV, and FASER2 at the HL-LHC can probe new parameter space for a wide range of HNL masses from 150 MeV to 4 GeV.

Additionally, we considered two new mixed-coupling benchmark models, 011 and 111, and determined the sensitivity of FASER and FASER2. These new benchmarks are not well studied and there are no comprehensive studies of the sensitivity of other current and proposed experiments in these models. We roughly estimated the sensitivity of past experiments and found that FASER2 at the HL-LHC can likely probe new parameter space for a wide range of HNL masses from 400 MeV to 4 GeV.

Overall, this study contributes significantly to the understanding of HNLs and their potential implications in particle physics. We produced `HNLCalc`, a flexible, fast, comprehensive, and publicly available tool for computing HNL decay and production rates with arbitrary couplings. In this study, we used this tool to extend the `FORESEE` simulation package to incorporate HNLs. Models with general HNL couplings are more complicated than models with a single coupling, but they are also more well motivated, and studies of the discovery prospects of other experiments in these models are encouraged.

ACKNOWLEDGMENTS

We are grateful to the authors and maintainers of many open-source software packages, including scikit-hep [53] and CRMC [54]. This work is supported in part by U.S. National Science Foundation (NSF) Grant No. PHY-2210283 and Simons Foundation Grant No. 623683. The work of J. L. F. is supported in part by NSF Grant

No. PHY-2111427, Simons Investigator Award No. 376204, and Heising-Simons Foundation Grant No. 2019-1179 and No. 2020-1840. F. K. acknowledges support by the Deutsche Forschungsgemeinschaft under Germany's Excellence Strategy—EXC 2121 Quantum Universe—390833306.

APPENDIX A: HNL PRODUCTION MODES

In this appendix, we present a comprehensive compilation of expressions for the leading processes for HNL production. Specifically, in the following five subsections we present the branching fractions for the processes $P \to lN$, $P \to P'lN$, $P \to VlN$, $\tau \to PN$, and $\tau \to \nu lN, \bar{\nu} lN$, where P and P' denote pseudoscalar mesons, V denotes vector mesons, l is a charged lepton, and N is the HNL. The decays implemented are shown in Table I.

1. Two-body pseudoscalar decays $P \to lN$

The two-body leptonic decays of pseudoscalar mesons into HNLs have branching fractions [18,21]

$$B(P \to l_\alpha N) = \tau_P |U_\alpha|^2 \frac{G_F^2 m_P m_N^2 |V_P|^2 f_P^2}{8\pi} \times \left[1 - \frac{m_N^2}{m_P^2} + 2\frac{m_l^2}{m_P^2} + \frac{m_l^2}{m_N^2}\left(1 - \frac{m_l^2}{m_P^2}\right)\right] \times \sqrt{\left(1 + \frac{m_N^2}{m_P^2} - \frac{m_l^2}{m_P^2}\right)^2 - 4\frac{m_N^2}{m_P^2}}, \tag{A1}$$

where $\alpha = e, \mu, \tau$, τ_P is the meson lifetime, U_α parametrizes the mixing with the active neutrino, and G_F is the Fermi constant. The decay constants f_P are given in Table IV, and V_P denotes the relevant Cabibbo-Kobayashi-Maskawa (CKM) matrix element; for example, for $P = \pi^+$, $V_P = V_{ud}$.

2. Three-body pseudoscalar decays $P \to P'lN$

For pseudoscalar mesons decaying semileptonically to pseudoscalar mesons, the differential branching fraction is [21]

$$\begin{aligned}\frac{dB(P \to P' l_\alpha N)}{dE_N dq^2} = \tau_P |U_\alpha|^2 \frac{G_F^2 |V_{PP'}|^2}{64\pi^3 m_P^2} c_P \{ & f_-^2(q^2) \cdot [q^2(m_N^2 + m_l^2) - (m_N^2 - m_l^2)^2] \\ & + 2 f_+(q^2) f_-(q^2)[m_N^2(2m_P^2 - 2m_{P'}^2 - 4E_N m_P - m_l^2 + m_N^2 + q^2) + m_l^2(4E_N m_P + m_l^2 - m_N^2 - q^2)] \\ & + f_+^2(q^2)[(4E_N m_P + m_l^2 - m_N^2 - q^2)(2m_P^2 - 2m_{P'}^2 - 4E_N m_P - m_l^2 + m_N^2 + q^2) \\ & - (2m_P^2 + 2m_{P'}^2 - q^2)(q^2 - m_N^2 - m_l^2)]\},\end{aligned} \tag{A2}$$

where $q^2 = (p_l + p_N)^2$, E_N is the HNL energy in the P c.m. frame, and $V_{PP'}$ is the appropriate CKM matrix element for the process (e.g., for $D^+ \to \bar{K}^0 l^+ N$, $V_{PP'} = V_{cs}$). The constant c_P and the form factors $f_-(q^2)$ and $f_+(q^2)$ are defined below. Equation (A2) corrects a minor typo in Eq. (B2) of Ref. [21], which was missing a plus sign. Additionally, we replace the masses m_K and m_π in Eq. (B2) of Ref. [21] with m_P and $m_{P'}$, respectively.

TABLE IV. Pseudoscalar and vector-meson decay constants used in this study.

P	f_P (MeV)	V	f_V (MeV)
π^0 [55]	130.3	ρ^0 [56]	220
π^+ [55]	130.3	ρ^+ [56]	220
K^+ [55]	156.4	ω [56]	195
η [57]	78.4	K^{*+} [55]	204
η' [57]	−95.7	ϕ [55]	229
D^+ [58]	222.6		
D_s^+ [59]	280.1		
B^+ [21]	190		
B_c^+ [21]	480		

To determine the branching fractions, we must integrate Eq. (A2) over the region [60]

$$\begin{aligned}(m_l + m_N)^2 \le q^2 \le (m_H - m_{H'})^2, \\ E_N(m_{NH'}^{2\,\min}, q^2) \le E_N \le E_N(m_{NH'}^{2\,\max}, q^2),\end{aligned} \tag{A3}$$

where

$$\begin{aligned}E_N(m_{NH'}^2, q^2) &= \frac{q^2 + m_{NH'}^2 - m_{H'}^2 - m_l^2}{2m_H}, \\ m_{NH'}^{2\,\min} &= (E_N^* + E_{H'}^*)^2 - \left(\sqrt{E_N^{*2} - m_N^2} + \sqrt{E_{H'}^{*2} - m_{H'}^2}\right)^2, \\ m_{NH'}^{2\,\max} &= (E_N^* + E_{H'}^*)^2 - \left(\sqrt{E_N^{*2} - m_N^2} - \sqrt{E_{H'}^{*2} - m_{H'}^2}\right)^2,\end{aligned} \tag{A4}$$

where $E_N^* = (m_{lN}^2 - m_l^2 + m_N^2)/2m_{lN}$, and $E_{H'}^* = (m_H^2 - m_{lN}^2 - m_{H'}^2)/2m_{lN}$ are the energies of N and H' in the c.m. frame of the $l - N$ system. Equation (A3) corrects a typo found below Eq. (2) of Ref. [61], where the q^2 dependence of the integration bounds for E_N was neglected.

The hadronic form factors $f_-(q^2)$ and $f_+(q^2)$ appearing in Eq. (A2) are defined by [61]

$$f_+(q^2) = \frac{f_+(0)}{(1 - q^2/m_{V'}^2)}, \tag{A5}$$

$$f_0(q^2) = \frac{f_0(0)}{(1 - q^2/m_S^2)}, \tag{A6}$$

$$f_0(q^2) = f_+(q^2) + \frac{q^2}{m_P^2 - m_{P'}^2} f_-(q^2). \tag{A7}$$

Here $m_{V'}$ and m_S are the masses of the vector and scalar resonances, respectively. These are determined from the quark transition of the decay (e.g., for $D^+ \to \bar{K}^0 l^+ N$, which involves a $c \to s$ quark transition, $m_{V'} = m_{D_s^{*+}}$, and $m_S = m_{D_s^+}$). It is important to note that $f_+(0)$ and $f_-(0)$ are determined by Eqs. (A5) to (A7) and therefore we only provide values for $f_0(0)$, which are listed in Table V.

The constants c_P are determined by the quark content of the initial- and final-state mesons. As an example, consider the decay $D^+ \to \eta l^+ N$, which depends on the matrix element $\langle \eta | \bar{d} \gamma^\mu P_L c | D^+ \rangle$. The quark content of η and η' is related to η_8 and η_1 through a rotation matrix:

$$\begin{pmatrix} \eta \\ \eta' \end{pmatrix} = \begin{pmatrix} \cos\theta_P & -\sin\theta_P \\ \sin\theta_P & \cos\theta_P \end{pmatrix} \begin{pmatrix} \eta_8 \\ \eta_1 \end{pmatrix}. \tag{A8}$$

Inserting $\eta_8 = (u\bar{u} + d\bar{d} - 2s\bar{s})/\sqrt{6}$ and $\eta_1 = (u\bar{u} + d\bar{d} + s\bar{s})/\sqrt{3}$, we obtain

$$\eta = \left(\frac{\cos\theta_P}{\sqrt{6}} - \frac{\sin\theta_P}{\sqrt{3}}\right) u\bar{u} + \left(\frac{\cos\theta_P}{\sqrt{6}} - \frac{\sin\theta_P}{\sqrt{3}}\right) d\bar{d} + \left(-\frac{2\cos\theta_P}{\sqrt{6}} - \frac{\sin\theta_P}{\sqrt{3}}\right) s\bar{s}. \tag{A9}$$

From this, we observe that the matrix element $\langle \eta | \bar{d} \gamma^\mu P_L c | D^+ \rangle$ is proportional to $(\frac{\cos\theta_P}{\sqrt{6}} - \frac{\sin\theta_P}{\sqrt{3}}) \langle d | \bar{d} \gamma^\mu P_L c | c \rangle$, where $\langle d | \bar{d} \gamma^\mu P_L c | c \rangle$ is the same matrix element encountered in the decay $D^0 \to \pi^- l^+ N$ and thus shares the same form factors. This implies that the parameter c_P for the decay $D^+ \to \eta l^+ N$ is $(\frac{\cos\theta_P}{\sqrt{6}} - \frac{\sin\theta_P}{\sqrt{3}})^2$. The values of c_P are listed in Table V.

TABLE V. Parameters $f_0(0)$ and c_P, which appear in the $P \to P' l N$ branching fraction expressions (A2) to (A7), where $\theta_P = -11.5°$ [62].

Decay channel	$f_0(0)$	c_P
$K^+ \to \pi^0$ [63]	0.970	1/2
$K_S \to \pi^+$ [64]	0.9636	1/2
$K_L \to \pi^+$ [64]	0.9636	1/2
$\bar{D}^0 \to \pi^+$ [65]	0.69	1
$\bar{D}^0 \to K^+$ [66]	0.747	1
$D^+ \to \pi^0$ [65]	0.69	1/2
$D^+ \to \eta$ [65]	0.69	$(\frac{\cos\theta_P}{\sqrt{6}} - \frac{\sin\theta_P}{\sqrt{3}})^2$
$D^+ \to \eta'$ [65]	0.69	$(\frac{\sin\theta_P}{\sqrt{6}} + \frac{\cos\theta_P}{\sqrt{3}})^2$
$D^+ \to \bar{K}^0$ [66]	0.747	1
$D_s^+ \to \bar{K}^0$ [66]	0.747	1
$D_s^+ \to \eta$ [67]	0.495	1
$D_s^+ \to \eta'$ [67]	0.557	1
$B^+ \to \pi^0$ [65]	0.29	1/2
$B^+ \to \eta$ [65]	0.29	$(\frac{\cos\theta_P}{\sqrt{6}} - \frac{\sin\theta_P}{\sqrt{3}})^2$
$B^+ \to \eta'$ [65]	0.29	$(\frac{\sin\theta_P}{\sqrt{6}} + \frac{\cos\theta_P}{\sqrt{3}})^2$
$B^+ \to \bar{D}^0$ [68]	0.66	1
$B^0 \to \pi^+$ [65]	0.29	1
$B^0 \to D^-$ [68]	0.66	1
$B_s^0 \to K^-$ [65]	0.31	1
$B_s^0 \to D_s^-$ [69]	−0.65	1
$B_c^+ \to D^0$ [70]	0.69	1
$B_c^+ \to \eta_c$ [70]	0.76	1
$B_c^+ \to B^0$ [70]	−0.58	1
$B_c^+ \to B_s^0$ [70]	−0.61	1

3. Three-body pseudoscalar decays $P \to V l N$

For pseudoscalar mesons decaying semileptonically to vector mesons, the differential branching fraction is [21]

$$\begin{aligned}
\frac{dB(P \to V l_\alpha N)}{dE_N dq^2} = \tau_P |U_\alpha|^2 \frac{G_F^2 |V_{PV}|^2}{32\pi^3 m_P} c_V \Bigg\{ & \frac{f_2^2}{2}\left(q^2 - m_N^2 - m_l^2 + \omega^2 \frac{\Omega^2 - \omega^2}{m_V^2}\right) + \frac{f_5^2}{2}(m_N^2 + m_l^2)(q^2 - m_N^2 + m_l^2)\left(\frac{\Omega^4}{4m_V^2} - q^2\right) \\
& + 2f_3^2 m_V^2 \left(\frac{\Omega^4}{4m_V^2} - q^2\right)\left(m_N^2 + m_l^2 - q^2 + \omega^2 \frac{\Omega^2 - \omega^2}{m_V^2}\right) \\
& + 2f_3 f_5 \left[m_N^2 \omega^2 + (\Omega^2 - \omega^2) m_l^2\right]\left(\frac{\Omega^4}{4m_V^2} - q^2\right) + 2f_1 f_2 \left[q^2(2\omega^2 - \Omega^2) + \Omega^2(m_N^2 - m_l^2)\right] \\
& + f_1^2 \left[\Omega^4(q^2 - m_N^2 + m_l^2) - 2m_V^2\left[q^4 - (m_N^2 - m_l^2)^2\right] + 2\omega^2\Omega^2(m_N^2 - q^2 - m_l^2) + 2\omega^4 q^2\right]\Bigg\} \\
& + \frac{f_2 f_5}{2}\left[\omega^2 \frac{\Omega^2}{m_V^2}(m_N^2 - m_l^2) + \frac{\Omega^4}{m_V^2} m_l^2 + 2(m_N^2 - m_l^2)^2 - 2q^2(m_N^2 + m_l^2)\right] \\
& + f_2 f_3 \left[\Omega^2 \omega^2 \frac{\Omega^2 - \omega^2}{m_V^2} + 2\omega^2(m_l^2 - m_N^2) + \Omega^2(m_N^2 - m_l^2 - q^2)\right],
\end{aligned} \tag{A10}$$

where $\omega^2 = m_P^2 - m_V^2 + m_N^2 - m_l^2 - 2m_P E_N$ and $\Omega^2 = m_P^2 - m_V^2 - q^2$. The constants c_V are conceptually identical to the constants c_P discussed in Sec. A 2.

The form factors are

$$f_1 = \frac{V}{m_P + m_V}, \tag{A11}$$

$$f_2 = (m_P + m_V)A_1, \tag{A12}$$

$$f_3 = -\frac{A_2}{m_P + m_V}, \tag{A13}$$

$$f_4 = [m_V(2A_0 - A_1 - A_2) + m_P(A_2 - A_1)]\frac{1}{q^2}, \tag{A14}$$

$$f_5 = f_3 + f_4. \tag{A15}$$

A_0 and V have the form

$$f(q^2) = \frac{f(0)}{(1 - q^2/m^2)(1 - \sigma_1 q^2/m^2 + \sigma_2 q^4/m^4)}, \tag{A16}$$

where $m = m_S$ for A_0 and $m = m_{V'}$ for V. A_1 and A_2 have the form

$$f(q^2) = \frac{f(0)}{(1 - \sigma_1 q^2/m_{V'}^2 + \sigma_2 q^4/m_{V'}^4)}. \tag{A17}$$

The parameters m_S and $m_{V'}$ are determined from the decay mode in a manner identical to $P \to P'lN$. The parameters σ_1 and σ_2 are unique for each of the form factors A_0, A_1, A_2, and V. A summary of the form factor parameters can be found in Table VI.

The form factors for certain B_c decays are a special case and all of the form factors A_0, A_1, A_2, and V are chosen to have the form [70]

$$f(q^2) = \frac{f(0)}{1 - q^2/m_{\text{fit}}^2 - \delta(q^2/m_{\text{fit}}^2)^2}, \tag{A18}$$

where δ and m_{fit} are fitting parameters unique to each of the form factors A_0, A_1, A_2, and V. These fitting parameters for the relevant decays can be found in Table VII.

4. Two-body tau decays $\tau \to PN$

The branching fraction for the $\tau \to PN$ decays is [21]

$$B(\tau \to PN) = \tau_\tau |U_\tau|^2 \frac{G_F^2 m_\tau^3 |V_P|^2 f_P^2}{16\pi} \times \left[\left(1 - \frac{m_N^2}{m_\tau^2}\right)^2 - \frac{m_P^2}{m_\tau^2}\left(1 + \frac{m_N^2}{m_\tau^2}\right)\right] \times \sqrt{\left(1 - \frac{(m_P - m_N)^2}{m_\tau^2}\right)\left(1 - \frac{(m_P + m_N)^2}{m_\tau^2}\right)}, \tag{A19}$$

where V_P is the CKM matrix element of P (e.g., if $P = \pi$, then $V_P = V_{ud}$). The τ lepton can also decay into a vector meson. In this case, the branching fraction is [21]

TABLE VI. Parameters $f_0(0)$, σ_1, σ_2, and c_V which appear in the $P \to VlN$ branching fraction expressions (A10) to (A17).

	A_0			A_1			A_2			V			
Decay channel	$f_0(0)$	σ_1	σ_2	$f_0(0)$	σ_1	σ_2	$f_0(0)$	σ_1	σ_2	$f(0)$	σ_1	σ_2	c_V
$D^0 \to \rho^-$ [65]	0.66	0.36	0	0.59	0.50	0	0.49	0.89	0	0.90	0.46	0	1
$D^0 \to K^{*-}$ [65]	0.76	0.17	0	0.66	0.3	0	0.49	0.67	0	1.03	0.27	0	1
$D^+ \to \rho^0$ [65]	0.66	0.36	0	0.59	0.50	0	0.49	0.89	0	0.90	0.46	0	1/2
$D^+ \to \omega$ [65]	0.66	0.36	0	0.59	0.50	0	0.49	0.89	0	0.90	0.46	0	1/2
$D^+ \to \overline{K^{*0}}$ [65]	0.76	0.17	0	0.66	0.3	0	0.49	0.67	0	1.03	0.27	0	1
$D_s^+ \to K^{*0}$ [65]	0.67	0.2	0	0.57	0.29	0.42	0.42	0.58	0	1.04	0.24	0	1
$D_s^+ \to \phi$ [65]	0.73	0.10	0	0.64	0.29	0	0.47	0.63	0	1.10	0.26	0	1
$B^+ \to \rho^0$ [65]	0.30	0.54	0	0.26	0.73	0.1	0.29	1.4	0.5	0.31	0.59	0	1/2
$B^+ \to \omega$ [65]	0.30	0.54	0	0.26	0.54	0.1	0.24	1.40	0.50	0.31	0.59	0	1/2
$B^+ \to \overline{D^{*0}}$ [65]	0.69	0.58	0	0.66	0.78	0	0.62	1.04	0	0.76	0.57	0	1
$B^0 \to \rho^-$ [65]	0.30	0.54	0	0.26	0.54	0.1	0.24	1.40	0.50	0.31	0.59	0	1
$B^0 \to D^{*-}$ [65]	0.69	0.58	0	0.66	0.78	0	0.62	1.04	0	0.76	0.57	0	1
$B_s^0 \to K^{*-}$ [65]	0.37	0.60	0.16	0.29	0.86	0.6	0.26	1.32	0.54	0.38	0.66	0.30	1
$B_s^0 \to D_s^{*-}$ [71]	0.67	0.35	0	0.70	0.463	0	0.75	1.04	0	0.95	0.372	0	1
$B_c^+ \to D^{*0}$ [70]	0.56	0	0	0.64	0	0	−1.17	0	0	0.98	0	0	1

TABLE VII. Parameters $f_0(0)$, δ, $m_{\rm fit}$, and c_V for certain $B_c \to VlN$ decays appearing in the branching fraction expressions (A10) and (A18).

	A_0			A_1			A_2			V			
Decay channel	$f_0(0)$	δ	$m_{\rm fit}$	$f_0(0)$	δ	$m_{\rm fit}$	$f_0(0)$	δ	$m_{\rm fit}$	$f(0)$	δ	$m_{\rm fit}$	c_V
$B_c^+ \to J/\psi$ [70]	0.68	1.40	8.20	0.68	0.052	5.91	−0.004	−0.004	5.67	0.96	0.0013	5.65	1
$B_c^+ \to B^{*0}$ [70]	−0.27	0.13	1.86	0.6	−1.07	3.44	10.8	−0.09	1.73	3.27	−0.052	1.76	1
$B_c^+ \to B_s^{*0}$ [70]	−0.33	0.13	1.86	0.4	−1.07	3.44	10.4	−0.09	1.73	3.27	−0.052	1.76	1

$$B(\tau \to VN) = \tau_\tau |U_\tau|^2 \frac{G_F^2 m_\tau^3 |V_V|^2 f_V^2}{8\pi}\left[\left(1-\frac{m_N^2}{m_\tau^2}\right)^2 + \frac{m_V^2}{m_\tau^2}\left(1+\frac{m_N^2-2m_V^2}{m_\tau^2}\right)\right] \times \sqrt{\left(1-\frac{(m_V-m_N)^2}{m_\tau^2}\right)\left(1-\frac{(m_V+m_N)^2}{m_\tau^2}\right)}, \tag{A20}$$

where V_V is the CKM matrix element for the corresponding vector meson. Note that in the literature this branching fraction is often written in terms of the coupling $g_V = m_V f_V$ [14].

5. Three-body tau decays $\tau \to \nu l N, \bar{\nu} l N$

Last, we consider three-body τ decays. The differential branching fractions are [21]

$$\frac{dB(\tau \to \nu_\tau l_\alpha N)}{dE_N} = \tau_\tau |U_\alpha|^2 \frac{G_F^2 m_\tau^2}{2\pi^3} E_N \left(1-\frac{m_l^2}{m_\tau^2+m_N^2-2E_N m_\tau}\right)\sqrt{E_N^2-m_N^2}\left(1+\frac{m_N^2-m_l^2}{m_\tau^2}-2\frac{E_N}{m_\tau}\right), \tag{A21}$$

and

$$\frac{dB(\tau \to \bar{\nu}_\alpha l_\alpha N)}{dE_N} = \tau_\tau |U_\tau|^2 \frac{G_F^2 m_\tau^2}{4\pi^3}\left(1-\frac{m_l^2}{m_\tau^2+m_N^2-2E_N m_\tau}\right)^2\sqrt{E_N^2-m_N^2} \times \left[(m_\tau - E_N)\left(1-\frac{m_N^2+m_l^2}{m_\tau^2}\right)-\left(1-\frac{m_l^2}{m_\tau^2+m_N^2-2E_N m_\tau}\right)\left(\frac{(m_\tau-E_N)^2}{m_\tau}+\frac{E_N^2-m_N^2}{3m_\tau}\right)\right], \tag{A22}$$

where $\alpha \neq \tau$. The bounds of integration are

$$m_N \leq E_N \leq \frac{m_\tau^2+m_N^2-m_l^2}{2m_\tau}. \tag{A23}$$

APPENDIX B: HNL DECAY RATES

HNL decays are induced by both CC and NC interactions. These interactions are a result of mixing with the SM neutrino gauge eigenstates, which can be seen in the following interacting Lagrangian:

$$-\mathcal{L}^{CC} = \frac{g}{\sqrt{2}}\sum_{\alpha=e,\mu,\tau} U_\alpha^* W_\mu^+ \overline{N^c}\gamma^\mu P_L l_\alpha + \text{H.c.}, \tag{B1}$$

$$-\mathcal{L}^{NC} = \frac{g}{2\cos\theta_W}\sum_{\alpha=e,\mu,\tau} U_\alpha^* Z_\mu \overline{N^c}\gamma^\mu P_L \nu_\alpha + \text{H.c.} \tag{B2}$$

In our analysis of HNL decays, we adopt the convention of Ref. [15], where decay rates are summed over all final neutrino mass eigenstates, giving the relationship

$$\Gamma(N \to \nu X) = \sum_{i=1,2,3}\Gamma(N \to \nu_i X) = \sum_{\alpha=e,\mu,\tau}\Gamma(N \to \nu_\alpha X) + \Gamma(N \to \overline{\nu}_\alpha X). \tag{B3}$$

The benefit of this choice is that it allows one to remain agnostic about whether light active neutrinos ν_α are treated as Dirac or Majorana particles [15], a convention choice that leads to nonphysical, factor-of-2 discrepancies throughout the literature [10–12,14,21].

1. Leptonic decays

HNLs decay into purely leptonic final states through the CC and NC processes shown in Figs. 3(a)–3(c). The decay widths are [16]

$$\Gamma(N \to \nu l_\alpha^- l_\alpha^+) = \frac{G_F^2 m_N^5}{96\pi^3} \sum_{\beta=e,\mu,\tau} |U_\beta|^2 [(C_1^l + 2\sin^2\theta_W \delta_{\alpha\beta}) f_1(x_\alpha) + (C_2^l + \sin^2\theta_W \delta_{\alpha\beta}) f_2(x_\alpha)], \tag{B4}$$

$$\Gamma(N \to \nu l_\alpha^- l_\beta^+) = \frac{G_F^2 m_N^5}{192\pi^3} [|U_\alpha|^2 I_1(0, x_\alpha^2, x_\beta^2) + |U_\beta|^2 I_1(0, x_\beta^2, x_\alpha^2)] \quad (\alpha \neq \beta), \tag{B5}$$

$$\Gamma(N \to \nu\bar{\nu}\nu) = \sum_{\alpha=e,\mu,\tau} \sum_{\beta=e,\mu,\tau} \Gamma_\pm(N \to \nu_\alpha \bar{\nu}_\beta \nu_\beta) = \frac{G_F^2 m_N^5}{96\pi^3} \left(\sum_{\alpha=e,\mu,\tau} |U_\alpha|^2 \right), \tag{B6}$$

where $x_i = \frac{m_i}{m_N}$, $C_1^l = (1 - 4\sin^2\theta_W + 8\sin^4\theta_W)/4$, and $C_2^l = (2\sin^4\theta_W - \sin^2\theta_W)/2$. The kinematic functions $f_1(x)$, $f_2(x)$, and $I_1(x, y, z)$ are given by

$$I_1(x, y, z) = 12 \int_{(\sqrt{x}+\sqrt{y})^2}^{(1-\sqrt{z})^2} \frac{ds}{s} (s - x - y)(1 + z - s) \lambda^{\frac{1}{2}}(1, x, y) \lambda^{\frac{1}{2}}(1, s, z), \tag{B7}$$

$$f_1(x) = (1 - 14x^2 - 2x^4 - 12x^6)\sqrt{1 - 4x^2} + 12x^4(x^4 - 1)L(x), \tag{B8}$$

$$f_1(x) = 4[x^2(2 + 10x^2 - 12x^4)\sqrt{1 - 4x^2} + 6x^4(1 - 2x^2 + 2x^4)L(x)], \tag{B9}$$

where

$$L(x) = \ln\left(\frac{1 - 3x^2 - (1 - x^2)\sqrt{1 - 4x^2}}{x^2(1 + \sqrt{1 - 4x^2})} \right), \tag{B10}$$

$$\lambda(x, y, z) = x^2 + y^2 + z^2 - 2xy - 2yx - 2xz. \tag{B11}$$

For $m_N < m_\pi$, the dominant decay is the invisible decay $N \to \nu\bar{\nu}\nu$. However, for $m_N > m_\pi$, the two-body semileptonic pion decay, $\nu\pi$, becomes kinematically accessible and begins to dominate the HNL decay width. This can be observed explicitly in Figs. 4 and 5.

2. Hadronic decays

a. Single-meson decay

HNL decays into hadronic final states occur through the NC and CC processes depicted in Figs. 3(d)–3(e). As mentioned in Sec. IV, for $m_N < 1.0$ GeV, the total hadronic width is calculated via decay into single-meson final states. The formulas for the decay of HNLs into single mesons are [16]

$$\Gamma(N \to \nu P^0) = \left(\sum_{\beta=e,\mu,\tau} |U_\beta|^2 \right) \frac{G_F^2 f_P^2 m_N^3}{16\pi} (1 - x_P^2)^2 \quad [P^0 = \pi^0, \eta, \eta'], \tag{B12}$$

$$\Gamma(N \to l_\alpha^\mp P^\pm) = |U_\alpha|^2 |V_{q\bar{q}}|^2 \frac{G_F^2 f_P^2 m_N^3}{16\pi} \lambda^{\frac{1}{2}}(1, x_P^2, x_\alpha^2)[1 - x_P^2 - x_\alpha^2(2 + x_P^2 - x_\alpha^2)] \quad [P^\pm = \pi^\pm, K^\pm, D^\pm, D_s^\pm], \tag{B13}$$

$$\Gamma(N \to \nu V^0) = \left(\sum_{\beta=e,\mu,\tau} |U_\beta|^2 \right) \frac{G_F^2 f_V^2 \kappa_V^2 m_N^3}{16\pi} (1 + 2x_V^2)(1 - x_V^2)^2 \quad [V^0 = \rho, \omega, \phi], \tag{B14}$$

$$\Gamma(N \to l_\alpha^\mp V^\pm) = |U_\alpha|^2 |V_{q\bar{q}}|^2 \frac{G_F^2 f_V^2 m_N^3}{16\pi} \lambda^{\frac{1}{2}}(1, x_V^2, x_\alpha^2)[(1 - x_V^2)(1 + 2x_V^2) + x_\alpha^2(x_V^2 + x_\alpha^2 - 2)] \quad [V^\pm = \rho^\pm, K^{*\pm}], \tag{B15}$$

where $\kappa_\rho = 1\text{–}2\sin^2\theta_W$, $\kappa_\omega = -2\sin^2\theta_W/3$, and $\kappa_\phi = -\sqrt{2}(1/2 - 2\sin^2\theta_W/3)$. The meson decay constants $f_{P,V}$ are given in Table IV.

b. Multimeson decays

In the regime $m_N > 1.0$ GeV, the total hadronic width is instead calculated via decays into quarks, since in this region decays into multimeson states become relevant to the total width. The tree-level NC and CC decays into quarks are given by [14]

$$\Gamma(N \to \nu q\bar{q}) = \left(\sum_{\beta=e,\mu,\tau} |U_\beta|^2\right) \frac{G_F^2 m_N^5}{32\pi^3} \times [C_1^q f_1(x_\alpha) + C_2^q f_2(x_\alpha)], \tag{B16}$$

$$\Gamma(N \to l_\alpha^- u\bar{d}) = \Gamma(N \to l_\alpha^+ \bar{u} d) = |U_\alpha|^2 |V_{ud}|^2 \frac{G_F^2 m_N^5}{64\pi^3} I_1(x_\alpha^2, x_u^2, x_d^2), \tag{B17}$$

where the coefficients C_1^q and C_2^q are given by

$$C_1^{u,c} = \frac{1}{4}\left(1 - \frac{8}{3}\sin^2\theta_W + \frac{32}{9}\sin^4\theta_W\right),$$
$$C_2^{u,c} = \frac{1}{3}\sin^2\theta_W\left(\frac{4}{3}\sin^2\theta_W - 1\right), \tag{B18}$$

$$C_1^{d,s,b} = \frac{1}{4}\left(1 - \frac{4}{3}\sin^2\theta_W + \frac{8}{9}\sin^4\theta_W\right),$$
$$C_2^{d,s,b} = \frac{1}{6}\sin^2\theta_W\left(\frac{2}{3}\sin^2\theta_W - 1\right). \tag{B19}$$

As is discussed in Refs. [14,16], the total hadronic width can be estimated using this tree-level decay along with a QCD loop correction that accounts for the hadronization process. This correction is estimated from hadronic tau decay. The loop corrections can be defined as

$$1 + \Delta_{\rm QCD} \equiv \frac{\Gamma(\tau \to \nu_\tau + \text{hadrons})}{\Gamma_{\rm tree}(\tau \to \nu_\tau u\bar{d}) + \Gamma_{\rm tree}(\tau \to \nu_\tau u\bar{s})}, \tag{B20}$$

where the correction up to $\mathcal{O}(\alpha_s^3)$ has been calculated to be

$$\Delta_{\rm QCD} = \frac{\alpha_s}{\pi} + 5.2\frac{\alpha_s^2}{\pi^2} + 26.4\frac{\alpha_s^3}{\pi^3}. \tag{B21}$$

We apply this correction to the NC decays $\nu q\bar{q}$ with $q = u$, d, s and the CC decays $lu\bar{d}$ and $lu\bar{s}$, where $\alpha_s = \alpha_s(m_N)$. The package rundec is used to compute the α_s running; see Ref. [72]. Additionally, for the decay νss, a phase-space suppression factor, $\sqrt{1 - 4m_K^2/m_N^4}$, is included to not overestimate this mode's contribution for $m_N < 2m_K$. This same approach is also applied to the decays τud and τus, with kinematic thresholds at $m_\tau + 2m_\pi$ and $m_\tau + m_\pi + m_K$, respectively.

3. HNL total decay width

The total decay width of the HNL is obtained by summing over all possible final-state decays. Since we are considering Majorana HNLs, the CC decays $N \to l_\alpha^+ H^-(\bar{u}d), \nu l_\alpha^+ l_\beta^-$ and their charge conjugates are both possible and, since they have equal decay rates, a factor of 2 must be included when calculating the total rate. In the region $m_N < 1.0$ GeV, the total decay width is

$$\Gamma_N = \Gamma(N \to \nu\bar{\nu}\nu) + \sum_{\alpha=e,\mu,\tau} \Gamma(N \to \nu l_\alpha^+ l_\alpha^-) + \sum_{P^0=\pi^0,\eta,\eta'} \Gamma(N \to \nu P^0) + \sum_{V^0=\rho^0,\omega,\phi} \Gamma(N \to \nu V^0) + \sum_{\alpha\neq\beta=e,\mu,\tau} 2\Gamma(N \to \nu l_\alpha^- l_\beta^+) + \sum_{\substack{P=\pi,K,D,D_s \\ \alpha=e,\mu,\tau}} 2\Gamma(N \to l_\alpha^- P^+) + \sum_{\substack{V=\rho,K^* \\ \alpha=e,\mu,\tau}} 2\Gamma(N \to l_\alpha^- V^+). \tag{B22}$$

For $m_N > 1.0$ GeV, this becomes

$$\Gamma_N = \Gamma(N \to \nu\bar{\nu}\nu) + \sum_{\alpha=e,\mu,\tau} \Gamma(N \to \nu l_\alpha^+ l_\alpha^-) + \sum_{q=u,d,s,c,b} \Gamma(N \to \nu q\bar{q}) + \sum_{\alpha\neq\beta=e,\mu,\tau} 2\Gamma(N \to \nu l_\alpha^- l_\beta^+) + \sum_{\substack{u=u,c \\ d=d,s,b}} 2\Gamma(N \to l_\alpha^- u\bar{d}). \tag{B23}$$

[1] M. Drewes, The phenomenology of right handed neutrinos, Int. J. Mod. Phys. E **22**, 1330019 (2013).
[2] F. F. Deppisch, P. S. Bhupal Dev, and A. Pilaftsis, Neutrinos and collider physics, New J. Phys. **17**, 075019 (2015).
[3] K. N. Abazajian, Sterile neutrinos in cosmology, Phys. Rep. **711–712**, 1 (2017).
[4] B. Dasgupta and J. Kopp, Sterile neutrinos, Phys. Rep. **928**, 1 (2021).
[5] J. D. Bjorken and C. H. Llewellyn Smith, Spontaneously broken gauge theories of weak interactions and heavy leptons, Phys. Rev. D **7**, 887 (1973).
[6] R. Shrock, Decay $L^0 \to \nu_l\gamma$ in gauge theories of weak and electromagnetic interactions, Phys. Rev. D **9**, 743 (1974).

[7] D. A. Bryman and R. Shrock, Constraints on sterile neutrinos in the MeV to GeV mass range, Phys. Rev. D **100**, 073011 (2019).

[8] T. Asaka and M. Shaposhnikov, The νMSM, dark matter and baryon asymmetry of the universe, Phys. Lett. B **620**, 17 (2005).

[9] R. E. Shrock, A test for the existence of effectively stable neutral heavy leptons, Phys. Rev. Lett. **40**, 1688 (1978).

[10] V. Gribanov, S. Kovalenko, and I. Schmidt, Sterile neutrinos in tau lepton decays, Nucl. Phys. **B607**, 355 (2001).

[11] A. Atre, T. Han, S. Pascoli, and B. Zhang, The search for heavy Majorana neutrinos, J. High Energy Phys. 05 (2009) 030.

[12] J. C. Helo, S. Kovalenko, and I. Schmidt, Sterile neutrinos in lepton number and lepton flavor violating decays, Nucl. Phys. **B853**, 80 (2011).

[13] M. Drewes and B. Garbrecht, Combining experimental and cosmological constraints on heavy neutrinos, Nucl. Phys. **B921**, 250 (2017).

[14] K. Bondarenko, A. Boyarsky, D. Gorbunov, and O. Ruchayskiy, Phenomenology of GeV-scale heavy neutral leptons, J. High Energy Phys. 11 (2018) 032.

[15] P. Ballett, T. Boschi, and S. Pascoli, Heavy neutral leptons from low-scale seesaws at the DUNE near detector, J. High Energy Phys. 03 (2020) 111.

[16] P. Coloma, E. Fernández-Martínez, M. González-López, J. Hernández-García, and Z. Pavlovic, GeV-scale neutrinos: Interactions with mesons and DUNE sensitivity, Eur. Phys. J. C **81**, 78 (2021).

[17] M. Ovchynnikov, J.-L. Tastet, O. Mikulenko, and K. Bondarenko, Sensitivities to feebly interacting particles: Public and unified calculations, Phys. Rev. D **108**, 075028 (2023).

[18] R. E. Shrock, New tests for, and bounds on, neutrino masses and lepton mixing, Phys. Lett. **96B**, 159 (1980).

[19] R. E. Shrock, General theory of weak leptonic and semi-leptonic decays. 1. Leptonic pseudoscalar meson decays, with associated tests for, and bounds on, neutrino masses and lepton mixing, Phys. Rev. D **24**, 1232 (1981).

[20] R. E. Shrock, General theory of weak processes involving neutrinos. 2. Pure leptonic decays, Phys. Rev. D **24**, 1275 (1981).

[21] D. Gorbunov and M. Shaposhnikov, How to find neutral leptons of the νMSM?, J. High Energy Phys. 10 (2007) 015; 11 (2013) 101(E).

[22] J. L. Feng, I. Galon, F. Kling, and S. Trojanowski, ForwArd search experiment at the LHC, Phys. Rev. D **97**, 035001 (2018).

[23] H. Abreu *et al.* (FASER Collaboration), The FASER detector, J. Instrum. **19**, P05066 (2024).

[24] L. A. Anchordoqui *et al.*, The forward physics facility: Sites, experiments, and physics potential, Phys. Rep. **968**, 1 (2022).

[25] J. L. Feng, F. Kling, M. H. Reno, J. Rojo, D. Soldin *et al.*, The forward physics facility at the high-luminosity LHC, J. Phys. G **50**, 030501 (2023).

[26] F. Kling and S. Trojanowski, Forward experiment sensitivity estimator for the LHC and future hadron colliders, Phys. Rev. D **104**, 035012 (2021).

[27] J. Beacham *et al.*, Physics beyond colliders at CERN: Beyond the standard model working group report, J. Phys. G **47**, 010501 (2020).

[28] F. Kling and S. Trojanowski, Heavy neutral leptons at FASER, Phys. Rev. D **97**, 095016 (2018).

[29] J. C. Helo, M. Hirsch, and Z. S. Wang, Heavy neutral fermions at the high-luminosity LHC, J. High Energy Phys. 07 (2018) 056.

[30] A. Ariga *et al.* (FASER Collaboration), FASER's physics reach for long-lived particles, Phys. Rev. D **99**, 095011 (2019).

[31] M. Drewes, J. Klarić, and J. López-Pavón, New benchmark models for heavy neutral lepton searches, Eur. Phys. J. C **82**, 1176 (2022).

[32] J.-L. Tastet and I. Timiryasov, Dirac vs. Majorana HNLs (and their oscillations) at SHiP, J. High Energy Phys. 04 (2020) 005.

[33] C. Antel *et al.*, Feebly-interacting particles: FIPs 2022 workshop report, Eur. Phys. J. C **83**, 1122 (2023).

[34] G. A. Vasquez and J. Zamora-Saa, Unveiling the heavy neutrino nature at LHCb, Phys. Rev. D **108**, 053008 (2023).

[35] M. V. Diwan, L. Anchordoqui, A. Ariga, T. Ariga, A. Barr *et al.*, Forward physics facility, https://www.osti.gov/biblio/1972463.

[36] T. Pierog, I. Karpenko, J. M. Katzy, E. Yatsenko, and K. Werner, EPOS LHC: Test of collective hadronization with data measured at the CERN Large Hadron Collider, Phys. Rev. C **92**, 034906 (2015).

[37] S. Alioli, P. Nason, C. Oleari, and E. Re, A general framework for implementing NLO calculations in shower Monte Carlo programs: The POWHEG BOX, J. High Energy Phys. 06 (2010) 043.

[38] C. Bierlich *et al.*, A comprehensive guide to the physics and usage of PYTHIA8.3, SciPost Phys. Codebases **2022**, 8 (2022).

[39] L. Buonocore, F. Kling, L. Rottoli, and J. Sominka, Predictions for neutrinos and new physics from forward heavy hadron production at the LHC, Eur. Phys. J. C **84**, 363 (2024).

[40] R. Mammen Abraham *et al.* (FASER Collaboration), Neutrino rate predictions for FASER, arXiv:2402.13318.

[41] S. Ostapchenko, Monte Carlo treatment of hadronic interactions in enhanced Pomeron scheme: I. QGSJET-II model, Phys. Rev. D **83**, 014018 (2011).

[42] F. Riehn, R. Engel, A. Fedynitch, T. K. Gaisser, and T. Stanev, Hadronic interaction model Sibyll 2.3d and extensive air showers, Phys. Rev. D **102**, 063002 (2020).

[43] H. Abreu *et al.* (FASER Collaboration), Search for dark photons with the FASER detector at the LHC, Phys. Lett. B **848**, 138378 (2024).

[44] FASER Collaboration, Search for axion-like particles in photonic final states with the FASER detector at the LHC, https://cds.cern.ch/record/2892328.

[45] H. Abreu *et al.* (FASER Collaboration), The FASER W-Si high precision preshower technical proposal, Technical Report, CERN, Geneva, 2022, https://cds.cern.ch/record/2803084.

[46] E. Fernández-Martínez, M. González-López, J. Hernández-García, M. Hostert, and J. López-Pavón, Effective portals to heavy neutral leptons, J. High Energy Phys. 09 (2023) 001.

[47] R. Barouki, G. Marocco, and S. Sarkar, Blast from the past II: Constraints on heavy neutral leptons from the BEBC WA66 beam dump experiment, SciPost Phys. **13**, 118 (2022).
[48] F. Bergsma *et al.* (CHARM Collaboration), A search for decays of heavy neutrinos in the mass range 0.5-GeV to 2.8-GeV, Phys. Lett. **166B**, 473 (1986).
[49] A. D. Dolgov, S. H. Hansen, G. Raffelt, and D. V. Semikoz, Heavy sterile neutrinos: Bounds from big bang nucleosynthesis and SN1987A, Nucl. Phys. **B590**, 562 (2000).
[50] A. Aguilar-Arevalo *et al.* (PIENU Collaboration), Improved search for heavy neutrinos in the decay $\pi \to e\nu$, Phys. Rev. D **97**, 072012 (2018).
[51] G. Aad *et al.* (ATLAS Collaboration), Search for heavy neutral leptons in decays of W bosons using a dilepton displaced vertex in $s = 13$ TeV pp collisions with the ATLAS detector, Phys. Rev. Lett. **131**, 061803 (2023).
[52] I. Boiarska, A. Boyarsky, O. Mikulenko, and M. Ovchynnikov, Constraints from the CHARM experiment on heavy neutral leptons with tau mixing, Phys. Rev. D **104**, 095019 (2021).
[53] E. Rodrigues *et al.*, The Scikit HEP Project—overview and prospects, EPJ Web Conf. **245**, 06028 (2020).
[54] R. Ulrich, T. Pierog, and C. Baus, Cosmic Ray Monte Carlo Package, CRMC, 10.5281/zenodo.5270381 (2021).
[55] Q. Chang, X.-N. Li, X.-Q. Li, and F. Su, Decay constants of pseudoscalar and vector mesons with improved holographic wavefunction, Chin. Phys. C **42**, 073102 (2018).
[56] D. Ebert, R. N. Faustov, and V. O. Galkin, Relativistic treatment of the decay constants of light and heavy mesons, Phys. Lett. B **635**, 93 (2006).
[57] T. Feldmann, Quark structure of pseudoscalar mesons, Int. J. Mod. Phys. A **15**, 159 (2000).
[58] M. Artuso *et al.* (CLEO Collaboration), Improved measurement of $B(D^+ \to \mu^+\nu)$ and the pseudoscalar decay constant f_{D^+}, Phys. Rev. Lett. **95**, 251801 (2005).
[59] S. Stone, Measurement of $D_s^+ \to \ell^+\nu$ and the decay constant F_{D_s}, Conf. Proc. C **060726**, 1032 (2006); arXiv: hep-ex/0610026v2.
[60] M. Tanabashi *et al.* (Particle Data Group), Review of particle physics. Kinematics, Phys. Rev. D **98**, 030001 (2018).
[61] E. Graverini, E. Van Herwijnen, and T. Ruf (SHiP Collaboration), Mass dependence of branching ratios into HNL for FairShip, https://cds.cern.ch/record/2133817.
[62] P. A. Zyla *et al.* (Particle Data Group), Review of particle physics, Prog. Theor. Exp. Phys. **2020**, 083C01 (2020).
[63] N. Carrasco, P. Lami, V. Lubicz, L. Riggio, S. Simula, and C. Tarantino, $K \to \pi$ semileptonic form factors with $N_f = 2 + 1 + 1$ twisted mass fermions, Phys. Rev. D **93**, 114512 (2016).
[64] S. Aoki, G. Cossu, X. Feng, H. Fukaya, S. Hashimoto, T. Kaneko, J. Noaki, and T. Onogi (JLQCD Collaboration), Chiral behavior of $K \to \pi l\nu$ decay form factors in lattice QCD with exact chiral symmetry, Phys. Rev. D **96**, 034501 (2017).
[65] D. Melikhov and B. Stech, Weak form-factors for heavy meson decays: An update, Phys. Rev. D **62**, 014006 (2000).
[66] N. Carrasco, P. Lami, V. Lubicz, E. Picca, L. Riggio, S. Simula, and C. Tarantino (ETM Collaboration), Scalar and vector form factors of $D \to \pi l\nu$ and $D \to Kl\nu$ decays with $N_f = 2 + 1 + 1$ Twisted femions, Proc. Sci., LATTICE2015 (**2016**) 261 [arXiv:1511.04877].
[67] G. Duplancic and B. Melic, Form factors of B, $B_s \to \eta^{(\prime)}$ and D, $D_s \to \eta^{(\prime)}$ transitions from QCD light-cone sum rules, J. High Energy Phys. 11 (**2015**) 138.
[68] H. Na, C. M. Bouchard, G. P. Lepage, C. Monahan, and J. Shigemitsu (HPQCD Collaboration), $B \to Dl\nu$ form factors at nonzero recoil and extraction of $|V_{cb}|$, Phys. Rev. D **92**, 054510 (2015); **93**, 119906(E) (2016).
[69] X. J. Chen, H. F. Fu, C. S. Kim, and G. L. Wang, Estimating form factors of $B_s \to D_s^{(*)}$ and their applications to semileptonic and non-leptonic decays, J. Phys. G **39**, 045002 (2012).
[70] M. A. Ivanov, J. G. Korner, and P. Santorelli, The semileptonic decays of the B_c meson, Phys. Rev. D **63**, 074010 (2001).
[71] R. N. Faustov and V. O. Galkin, Weak decays of B_s mesons to D_s mesons in the relativistic quark model, Phys. Rev. D **87**, 034033 (2013).
[72] F. Herren and M. Steinhauser, Version 3 of RunDec and CRunDec, Comput. Phys. Commun. **224**, 333 (2018).